SEGMENTED NANO-FORCE SENSOR

By

Gautham Dharuman

A THESIS

Submitted to
Michigan State University
in partial fulfillment of the requirements
for the degree of

Electrical Engineering – Master of Science

2013

ABSTRACT

SEGMENTED NANO-FORCE SENSOR

By

Gautham Dharuman

Nanoscale force sensors are finding widespread applications in atomic and biological force sensing where forces involved range from zeptonewtons to several nanonewtons. Different methods of nanoscale force sensing based on optical, electrical or purely mechanical schemes have been reported. However, each technique is limited by factors such as large size, low resolution, slow response, force range and alignment issues. In this research, a new device structure which could overcome the above mentioned constraints is studied theoretically and experimentally for the possibility of its application in nano-scale force sensing.

ACKNOWLEDGEMENTS

First of all, I wish to express my deepest gratitude to my research advisor, Professor Lixin Dong for his patience and encouragement throughout the period of my research. I am especially grateful for his open mindedness to new ideas and his constant guidance that helped me pursue research as a motivated student. Without his support, I do not think this thesis would have been possible.

I am grateful to my committee members, Prof. Vladimir Zelevinsky, Prof. John Verbonceur and Prof. Andrew Christlieb for their valuable suggestions and comments on my research. I also express my appreciation to Dr. Xudong Fan for his excellent guidance with TEM. I feel lucky to have been able to pursue a combined theoretical and experimental work during my study.

I would also like to thank my co-workers Mr. Fan Zheng, Mr. Miao Yu and Miss. Chinwe Nyenke for their help and motivation especially at times of need. I enjoyed working with them. Special thanks to Mr. Fan Zheng who helped me to a great extent with the experiments.

Finally, I would like to thank my family members who spent extensive time and effort to support and encourage me which was vital for the completion of this study. I pay my respect for their immeasurable love and understanding.

TABLE OF CONTENTS

LIST OF FIGURES	vi
Chapter 1 Overview	1
Chapter 2 Modeling: Mechanical Behavior and Tunneling Current	5
2.1 Elastic Buckling of Nanowires: A Beam Model	6
2.1.1 Surface effects and their Influence on Beam Deformation	6
2.1.2 Determining Angle of Rotation	13
2.1.3 Closed Form Solution for Force-Separation Relation	14
2.1.4 Incorporation of Surface Effects for Small Deflection Angles	16
2.2 Tunneling Current	17
2.2.1 MIM Model	17
2.3 Sensitivity of the Force Sensor	19
Chapter 3 Numerical Results	20
3.1 Effect of Force on Separation	20
3.2 Effect of Separation Change on the Tunneling Current	22
3.2 Effect of Buckling Force on the Tunneling Current – A Combined Model	22
3.4 Sensitivity Curve	24
3.5 Dimensional Variations: Effect of Length, Outer and Inner Diameter	25
Chapter 4 High Resolution Imaging and Elemental Detection	30
4.1 High Resolution Transmission Electron Microscopy (HRTEM)	30
4.1.1 Weak Phase Object Approximation (WPOA)	31
4.1.2 Phase Contrast from the Lens	32
4.2 Elemental Detection: X-EDS, STEM-XEDS, EELS, EFTEM	35
4.2.1 X-ray Energy Dispersive Spectroscopy (X-EDS)	36
4.2.2 Scanning Transmission Electron Microscopy (STEM):	39
4.2.3 Electron Energy Loss Spectroscopy (EELS)	45
4.2.4 Flemental Manning Using FETEM	49

Chapter 5 Electro-Mechanical Characterization and Model Verification	52
5.1 Buckling Experiment	52
5.2 Model Verification	55
Chapter 6 Quantum Transport: An Effective Non-Hermitian Hamiltonian Appr	oach 59
Chapter 7 Conclusions and Future Work	71
REFERENCES	74

LIST OF FIGURES

Figure 2.1 Segmented nano-structure buckled under the action of external force. Opposite directions of rotation causes the lower edges of the pods to move closer. For the interpretation of references to color in this and all other figures, the reader is referred to the electronic version of this thesis
Figure 2.2 Cross-sectional view of the nanowire of diameter D and surface layer thickness t 7
Figure 2.3 Distributed transverse load along the nanowire length due to residual surface stress 7
Figure 2.4 Half section of the beam (without the effect of residual surface tension)
Figure 2.5 Element of infinitesimal length between two cross sections normal to the original axis of the beam
Figure 2.6 Schematic of the deflection of an embedded nanoparticle
Figure 2.7 Equilibrium potential profile of the junction. E_F is the Fermi energy of the metal, W_F is its work function and φ is the equilibrium barrier height as seen by the electrons in the metal.
Figure 3.1 Force-Separation (F- δ) curve. Here, the Young's modulus is 100 GPa, the diameter of the nanowire is 20 nm, the diameter of the pod is 7.5 nm, and the length of the nanowire is 800 nm.
Figure 3.2 External force induced enhancement in tunneling current
Figure 3.3 Sensitivity values for the force range considered
Figure 3.4 A greater drop in separation along with shifted and increased force range is observed for smaller length
Figure 3.5 Cross section of the device structure with outer diameter D and inner diameter d and Young's modulus E ₁ and E ₂ respectively

Figure 3.6 a) Relation between force and separation change and b) relation between force and current density for inner diameters 8nm (blue), 7.5nm (red) and 7nm (pink) are plotted for α values from five to eighty degrees. Outer diameter fixed at 20nm
Figure 3.7 Relation between the maximum current density and the inner diameter
Figure 4.1 Schematic of image formation by atomic number contrast and mass-thickness contrast
Figure 4.2 (a) Phase distortion function vs. u and (b) Contrast transfer function vs. u [31] 33
Figure 4.3 HRTEM images of a section of the heterostructured nanowire at magnification (a) 600K (b) 800K (c) 1.2M (d) 1.5M. Lattice fringes are observed in every image
Figure 4.4 Schematic of the characteristic X-ray emission
Figure 4.5 (a) A high magnification picture of the heterostructured nanowire and (b) X-ray EDS obtained from the corresponding region
Figure 4.6 (a) Bright Field (BF) STEM image and (b) Dark Field (DF) STEM image of the heterostructured nanowire
Figure 4.7 (a) Image of a section of the heterostructured nanowire with X-EDS collected along the line (yellow) with the corresponding elemental profile for Nickel (green), Boron (blue) and Carbon (red). (b) Enlarged elemental profile of Nickel
Figure 4.8 (a) Line scans across two adjacent nanoparticles. (b) Corresponding concentration of Nickel (red), Boron (green) and Carbon (blue) appended to one another for comparison
Figure 4.9 (a) Image of a section of the heterostructured nanowire with X-EDS collected along the line (yellow) with the corresponding elemental profile for Nickel (blue), Boron (red) and Carbon (green). (b) and (c) show the enlarged elemental profiles along with the X-ray counts for Boron and Carbon respectively
Figure 4.10 (a) Image of a section of the heterostructured nanowire with X-EDS collected from the entire area. (b), (c) and (d) show the area maps of Nickel, Carbon and Boron respectively 44
Figure 4.11 A typical core energy loss spectrum for Nickel after background subtraction 46

Figure 4.12 (a) Dark field STEM image of a cluster of the heterostructured nanowires. (b) High loss spectrum around the ionization edge of Nickel (865eV) from the region marked in red in (a)
Figure 4.13 (a) Zero loss image of a heterostructured nanowire. Elemental maps of (b) Boron (c) Carbon and (d) Nickel obtained using the three window EFTEM method (e) color map of all three elements.
Figure 5.1 A SEM image showing a cluster of the segmented nanowires
Figure 5.2 Schematic showing the end displacement
Figure 5.3 TEM images during different stages of the electro-mechanical characterization 54
Figure 5.4 Experimental Current-Displacement% curve
Figure 5.5 Predicted Current-Displacement% curve for Ni-B ₄ C-Ni segmented nanowire 56
Figure 5.6 (a) Segmented nanostructure for small end displacement (b) same structure for large end displacement
Figure 6.1 Segmented nanostructure with discrete energy levels is assigned to subspace P while the leads with continuum levels are assigned to subspace Q
Figure 6.2 Potential profile of the structure before deformation. All barriers have equal width The ends correspond to the barrier between the leads (continuum states) and the end pot structures.
Figure 6.3 Resonance structure for (a) small coupling (b) Superradiance
Figure 6.4 Integrated transmission vs. the separation between the center pods
Figure 6.5 Eigenenergy trajectories in the complex plane for N=5, 13 and 101 as the center pods separation is changed from 0.3nm to 0.1nm.

Figure 6.6 (a) Eigenstates for a closed system (b) Eigenstates for the system coupled to the continuum at superradiance transition – superradiant states formed at the edges (c) Eigenstates for the open system with center pods separation decreased from superradiance value – a highly localized state is visible (d) Eigenstates for the open system with center pods separation increased from superradiance value – eigenstates decoupled from the left and the right half of the
system. 67
Figure 6.7 Superradiant state for (a) increased pod separation (b) Anderson Localization [40] 68
Figure 6.8 (a) Superradiance without disorder. Level repulsion increases as the center pod separation is decreased to (b) 0.17nm (c) 0.15nm (d) 0.13nm (e) 0.11nm (f) 0.1nm

Chapter 1

Overview

Nanoscale force sensors are finding widespread applications in atomic and biological force sensing [1, 2], the domains where forces involved range from zeptonewtons to several nanonewtons. Force exerted by a single nuclear spin is on the order of zeptonewtons [3] while that exerted by a single electron spin is about a thousand times larger [1]. Sensing single electron or nuclear spin forces is employed for three dimensional imaging of macromolecules such as proteins with atomic resolution [4]. Forces exerted by a single cell or molecular units within the cell could be in the order of a few pico-Newton (pN) [5] and their measurement might require a near-single molecular force resolution.

Different mechanisms of nanoscale force sensing have been reported. To mention a few are optical, electrical and purely mechanical methods. The optical system involves detecting the deflection of a light beam caused by the displacement of the sensing unit on application of the force [2]. In case of electro-mechanical coupling, the force sensing unit is coupled to a strain transducer which converts the strain into an electrical signal [6]. In a purely mechanical framework force sensing involves correlation with a visual measurement of the displacement [7]. Apart from the magnitude of force being sensed, the other important factors are force range and the corresponding sensitivity. Some applications require a single sensor to measure a wide range of forces varying over two or three orders of magnitude. For example, while measuring the force imparted by a biological cell the initial contact force can be a few pNs but as the cell evolves the force could be as high as tens of nNs [7]. The sensitivity of force measurement is of vital importance when very small changes in force are required to be detected, for example, changes

in force as a DNA molecule unzips or when a neighboring cell comes in contact with a cell that is already being sensed. Such processes involve changes in the force values in the order of pN and nN respectively. Therefore, sensors with highly non-linear variation between the force and the output signal are required for such applications. Though piezoelectric force sensors have very good sensitivity [8], the variation between the force applied and the current measured is linear ruling out their application for measuring small changes in force. Force sensors based on electron tunneling effect serve as potential candidates for this purpose. Since the tunneling current has an exponential relation with the separation between the units across which tunneling occurs, even a linear effect of force on the separation will have an exponential enhancement in output current thereby ensuring a non-linear variation between the force and the output signal. A piezotronic effect based nanoscale force sensor [9] is reported to have such non-linear variation since the effect is based on the tunneling of electrons through a schottky barrier. Sensitivity values in the order of 0.5-2pA/nN in a force range of 16-80nN are reported. Although this seems very attractive for the application, this sensor is based on the tunneling between a metallic AFM tip and a semiconducting nanowire. This restricts sensing to objects that are only metallic in nature. Therefore, it is required to design a sensor which makes use of the non-linear effect of tunneling while being independent of the electrical property of the object being sensed. It must be noted that although tunneling based force sensors can offer non-linear variation and therefore ultrahigh sensitivity, their working would critically depend on the alignment between the units across which tunneling occurs because a small error in the separation will cause a significant change in the force values reported. This is a limiting factor in Scanning Tunneling Microscope (STM) based force sensors which make use of the tunneling effect. Therefore, alignment is an important design aspect which has to be considered while designing such sensors. Moreover, such a device

structure would also offer the following advantages when compared to the optical nanoscale force sensors where the displacement transduction systems are optical: scalability to very small dimensions far below the optical wavelength, measurement without optical perturbation of susceptible samples and implementation as large array technologies with portable sensing [2]. The requirements of being alignment free, compact, of small volume (nano-scale dimensions) and incorporating tunneling effect for sharp rise in current could be met by a segmented nanowire which is of interest in this study. The structure resembles a 'peapod' structure with nanoparticles embedded within a nanowire. Preliminary experiments of buckling the segmented structure under constant applied DC voltage using nanorobotic manipulators showed sharp rise in the measured current as deformation increased. This led to the initial speculation that such a nonlinear rise in current could be as a result of tunneling effect. However, since the composition of the material was unclear X-ray Energy Dispersive Spectroscopic (X-EDS) studies and Electron Energy Loss Spectroscopic (EELS) studies were carried out in a Transmission Electron Microscope (TEM) to have a reasonable estimate of the composition of the structure. Results indicated that the structure could be composed of Nickel nanoparticles embedded within a Boron-Carbide nanowire. Boron-Carbide being insulating it was reasonable to assume that tunneling takes place between the metallic Nickel regions. However, the complex nature of the experiment made it difficult to observe the nature of strain induced by the buckling force. Hence, a simple mechanical model was developed for the case of pure buckling and the nature of change which could result in the sharp rise in current was studied. This model was coupled with a model for the tunneling current through the structure to study if the observed response could be predicted. The model predicted a non-linear rise in current with increasing force thereby serving the desired requirements in principle. However, the prediction did not match with the observed

results. A significant deviation was observed for large deformation. The reason for this deviation was identified by performing a separate experiment and the inapplicability of the model in the limit of this deviation was explained. Taking the cue from this deviation, the same condition was analyzed in the case of quantum transport i.e. assuming that the wave nature of the electron was preserved throughout the structure. This assumption is valid in the limit of ballistic transport which is possible in case of smaller dimensions of the structure. Therefore, a theoretical study was undertaken using the effective non-Hermitian Hamiltonian approach to determine the total transmission through the segmented structure under different conditions of disorder induced by the force. Surprising results were obtained and the possible reasons for the unexpected results are explained. An interesting parallel is drawn with the known case of Anderson localization [10] and the specific condition seen in the segmented structure is termed as an 'embryo' of Anderson localization for the same reason. The condition under study being a consequence of the external force, the system could serve as a model for force induced 'controlled' disorder – a concept which is widely studied in quantum information systems. To have a better understanding of the effect, the resonance structure is considered for some cases and its evolution w.r.t. the disorder is studied. To have a quantitative idea of the disorder, the trajectories of the eigenenergies were plotted on the complex plane and a common pattern was observed for longer structures as well. Finally, to gain insight into the surprising behavior the eigenstates were determined for conditions before and after deformation. A highly localized state was observed for the case of decrease in separation while for the separation increase states decoupled from left or right were observed. Though the effects seem very different in their nature, the reason for the symmetric drop in integrated transmission is qualitatively explained.

Chapter 2

Modeling: Mechanical Behavior & Tunneling Current

The mechanical change assumed to cause the non-linear rise in current can be schematically depicted as shown in figure 2.1. The action of force buckles the nanowire which causes the pods on either side of the center line to rotate in opposite direction. This rotation is expected to have a pronounced effect on the separation between the lower edges of the center pods. This chapter presents the mechanical and electrical model to correlate the external force applied to the current through the nanowire. The first part details the mechanical model used to obtain the relation between the force and the change in separation between the metallic regions. The second part discusses the tunneling current model which relates the separation change to the current. Finally, a brief note on the sensitivity of the structure as a force sensor is presented.

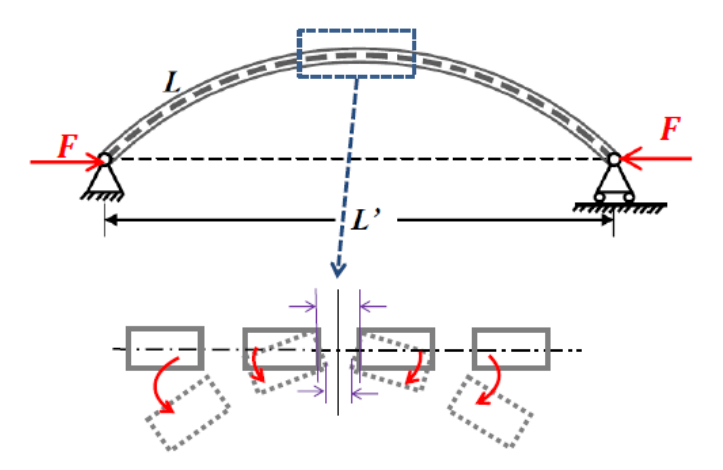


Figure 2.1 Segmented nano-stucture buckled under the action of external force. Opposite directions of rotation causes the lower edges of the pods to move closer. For the interpretation of references to color in this and all other figures, the reader is referred to the electronic version of this thesis.

2.1 Elastic Buckling of Nanowires: A Beam Model

Buckling characteristics of nanowires has been shown to be size dependent [11]. The dependence is due to the increasing influence of surface elasticity and residual stress with decreasing size [12]. Timoshenko beam model was adopted in [11] to explain the buckling dynamics of a nanowire incorporating surface effects and shear deformation. However, for high aspect ratio (large length/diameter ratio) nanowires the effect of shear deformation is negligible as shown in [11] and the classical Euler-Bernoulli beam theory [13] modified to incorporate surface effects has been shown to capture the details of the nanowire buckling and the relation with buckling force. In this work the nanowires of interest have large aspect ratios justifying their mechanical analysis without shear deformation. The details of the model are described in the following sections.

2.1.1 Surface effects and their Influence on Beam Deformation

Surface effects on the mechanical behavior of nano-scale materials can be incorporated through the surface elasticity and the residual surface stress. This is done through the surface stress tensor [14, 15] which for one dimensional case takes the form

$$\sigma^{s} = \tau + E^{s} \varepsilon^{s} \tag{2.1}$$

where τ is the residual surface stress and E^s is the surface stiffness. The surface elastic modulus can be determined experimentally or through atomistic simulations [16, 17]. A very thin isotropic elastic layer beneath the surface is used to model the surface elasticity. If the young's modulus of the surface layer is denoted as E_1 and its thickness as t then in accordance with the surface elasticity theory letting $t \to 0$ results in $E_1 t$ as the constant of surface stiffness E^s . In the

classical Euler-Bernoulli beam theory the flexural rigidity plays an important role in the deformation analysis. Cross sectional view of the nanowire is show in figure 2.2.

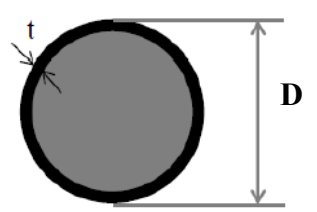


Figure 2.2 Cross-sectional view of the nanowire of diameter D and surface layer thickness t.

The flexural rigidity is given by EI where E is the Young's modulus of the bulk and I is the second moment of area which takes the form

$$I = (\pi E D^4)/64 \tag{2.2}$$

for a beam with circular cross section of diameter D. The effect of surface stiffness on the beam bending is included by modifying the form of flexural rigidity, in accordance with [18-20], into an effective flexural rigidity given by

$$(EI)^* = ((\pi E D^4)/64) + ((\pi E^s D^3)/8)$$
 (2.3)

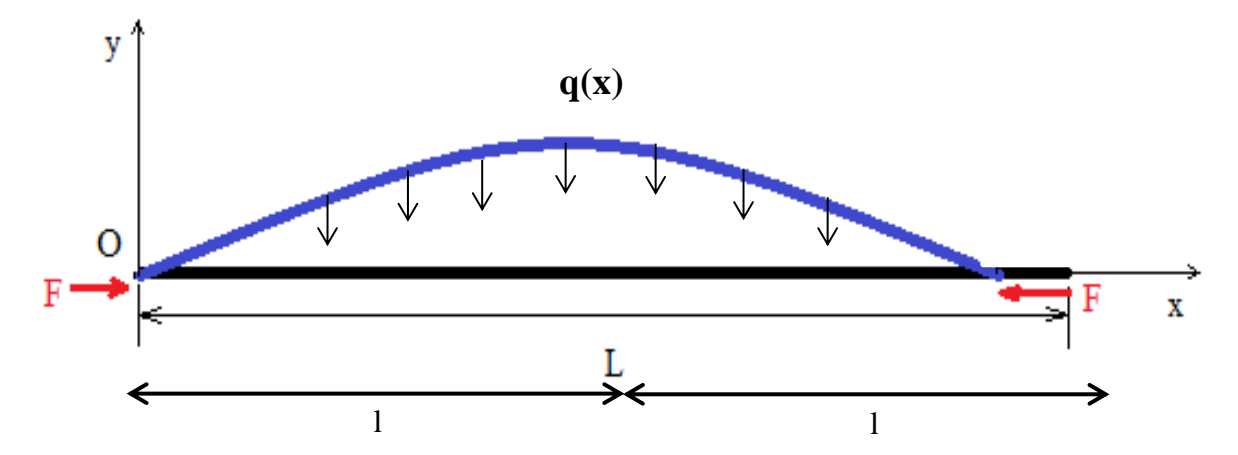


Figure 2.3 Distributed transverse load along the nanowire length due to residual surface stress.

In the deformed configuration the residual surface stress induces a distributed transverse load q(x) spanning the beam (as shown in figure 2.3) which according to Laplace-Young equation depends on the curvature [18, 19] as

$$q(x) = H * curvature (2.4)$$

where H is a constant determined by the residual surface stress and the cross sectional shape

$$H = 2\tau D \tag{2.5}$$

When subjected to an axial force F the beam deforms (buckles) and the steady state configuration takes the form as shown in figure 2.3. It must be noted that the axial force applied must exceed a certain value of force referred to as the critical force F_{cr} to induce deformation. Below the critical force no buckling occurs. Essentials of the structural equilibrium analysis follow the discussion in [21], with the modification to include surface effects in the final equation for the curvature of the buckled beam, is presented as follows. Consider a half section of the beam depicted in figure 2.3. A separate view of this section with a modified orientation of the coordinate axes is shown in figure 2.4.

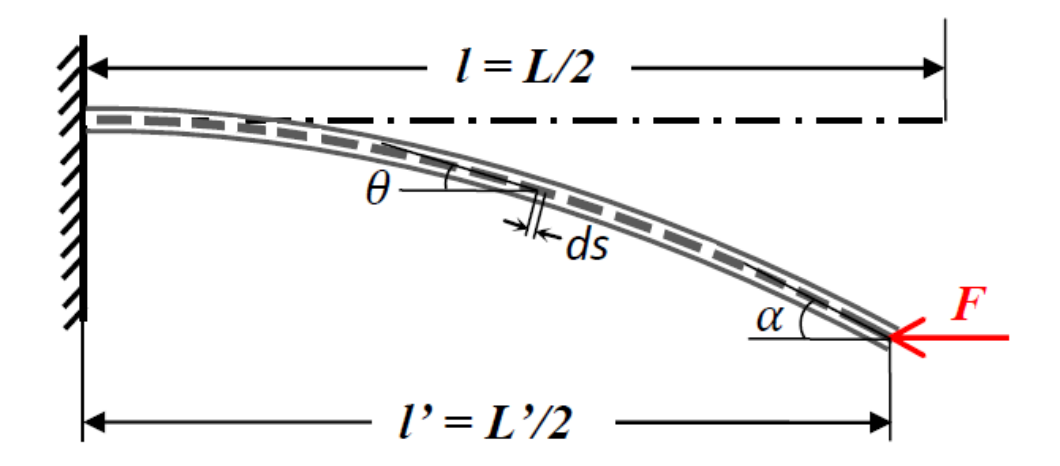


Figure 2.4 Half section of the beam (without the effect of residual surface tension).

An element of length *ds* between two cross sections taken normal to the original axis is considered. The moments and forces acting on this cross section are depicted in figure 2.5.

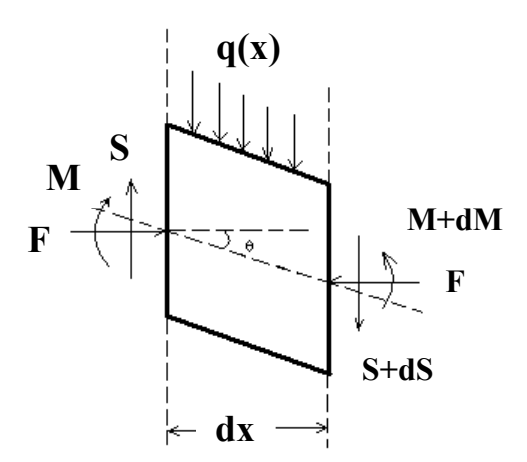


Figure 2.5 Element of infinitesimal length between two cross sections normal to the original axis of the beam.

Using the more accurate expression for curvature would yield the value of deflection without any ambiguity. The accurate expression relating the effective flexural rigidity with the moment is

$$(EI)^* (d\theta/ds) = -M \tag{2.6}$$

Force balance and moment balance conditions along with equation 2.6 results in

$$(1/2)(EI)^* (d\theta/ds)^2 = F \cos\theta - (1/2) \tau D \cos 2\theta - C \sin\theta + C'$$
 (2.7)

The boundary conditions to determine C and C are the curvatures becoming zero at the ends of the deformed wire i.e. at the terminal deflection angle as shown in figure 2.4. Solving for C and C from the boundary conditions gives

$$C = 0, C' = -F\cos\alpha + (1/2)\tau D\cos 2\alpha$$

Substituting for C and C' in equation 2.7 gives the final expression for the curvature as

$$d\theta/ds = \sqrt{(2/(EI)^*)[F(\cos\theta - \cos\alpha) - (1/2)\tau D(\cos2\theta - \cos2\alpha)]} \quad (2.8)$$

It is valid to assume that the central axis remains unchanged in its length [21]. Integrating ds gives the original length of the beam. Since the beam is symmetric, integration over the half integral $(0,\alpha)$ would suffice to understand the post-buckling state of the entire beam. If the effect of the residual surface stress is negligible i.e. if τ and E^s , equation 2.8 reduces to a form

$$ds = (1/k) (1/\sqrt{2(\cos\theta - \cos\alpha)})d\theta$$
 (2.9)

where
$$k = \sqrt{(F/EI)}$$
 (2.10)

and the expression is similar to the curvature equation obtained in [21]. For the sake of a simple theoretical demonstration of the device concept the simplified form of curvature (equation 2.9) is adopted by assuming the surface effects to be negligible. A complete analysis incorporating all the surface effects could be possible. As stated before any change in the axis length due to

compression is neglected. Therefore, integrating equation 2.9 from the limits $\theta = 0$ to α would give the half length l of the beam.

$$l = (1/k) \int_0^\alpha (1/\sqrt{2(\cos\theta - \cos\alpha)}) d\theta$$
 (2.11)

Following some trigonometric manipulations of the integrand, the half-length of the beam takes the form

$$l = K(p)/k (2.12)$$

where

$$K(p) = \int_0^{\pi/2} (1/\sqrt{1 - p^2 \sin^2 \Phi}) d\Phi$$
 (2.13)

is the complete elliptic integral of first kind with $p=\sin(\alpha/2)$ and $p \sin \varphi = \sin(\theta/2)$.

A similar analysis leads to the expressions for coordinates of the points on the deformed axis in terms of the applied force as follows

$$x = \sqrt{F/EI} \left[2E(\Phi, p) - F(\Phi, p) \right] \tag{2.14}$$

$$y = \sqrt{F/EI} \, 2p \, (1 - \cos \Phi) \tag{2.15}$$

where $F(\Phi, p)$ and $E(\Phi, p)$ are the incomplete elliptic integrals of first and second kind respectively. They take the form

$$F(\Phi, p) = \int_0^{\Phi} (1/\sqrt{1 - p^2 \sin^2 \Phi}) d\Phi$$
 (2.16)

$$E(\Phi, p) = \int_0^{\Phi} \sqrt{1 - p^2 \sin^2 \Phi} \ d\Phi$$
 (2.17)

Using equations 2.16 and 2.17, coordinates of the points on the deformed axes corresponding to different axial loads were determined by computing the incomplete elliptic integrals. Although numerical methods are available for evaluating the elliptic integrals [23], theta functions [24] were used to evaluate the value of the integrals to possibly obtain a physical understanding of the mechanical behavior.

Consider the schematic shown in figure 2.6.

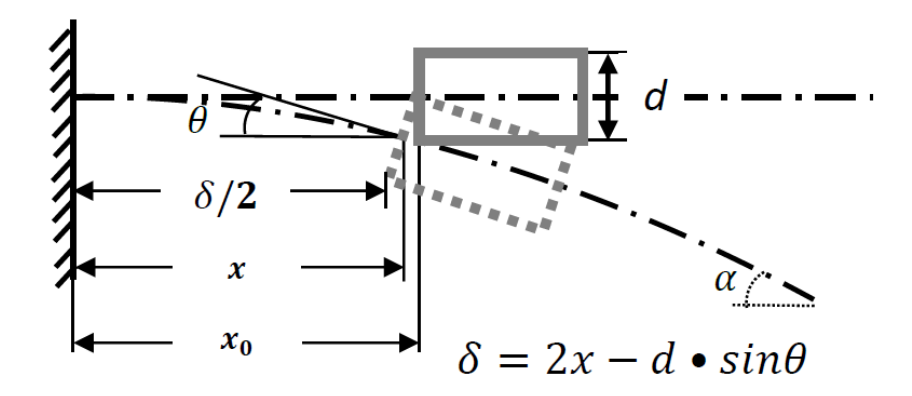


Figure 2.6 Schematic of the deflection of an embedded nanoparticle.

The cross-sectional planes are assumed to be rigid. Geometric analysis results in the expression for half spacing δ between the lower edges of the nanoparticles

$$\delta = 2x - dsin\theta \tag{2.18}$$

where x is the coordinate of the point of interest on the deformed axis and θ is the angle corresponding to the point. α is the terminal deflection angle. In order to determine δ it is

required to determine x and θ . Using equation 2.24, x can be determined if θ is known. Therefore, the first step is to determine the angle of rotation which requires further analysis.

2.1.2 Determining Angle of Rotation

Determination of θ requires the condition that x_0 is known. Theoretically for the case of pure buckling, compression of the axis is negligible. This implies that the axial separation between the nanoparticles maintains a constant value even as the force increases i.e. x_0 remains unchanged. However, this is not a strict condition. Even if x_0 changed with force, if the values can be determined from experiments or empirically, a similar analysis can be performed. The known value of x_0 can be formally related to Φ using equation 2.16

$$x_0 = \int_0^\theta ds = \int_0^\Phi (1/\sqrt{1 - p^2 sin^2 \Phi}) d\Phi$$
 (2.19)

where p $\sin \phi = \sin(\theta/2)$.

From equations 2.12, 2.16 and 2.19

$$x_0 = l(F(\Phi, p)/E(\Phi, p)) => F(\Phi, p)l = K(p) x_0$$
 (2.20)

 $F(\Phi, p)$ being denoted by u, the identity relating u and Φ is

$$sin\Phi = sn(u) \tag{2.21}$$

where sn(u) is the Jacobian elliptic sine function [24]. Therefore, Φ can be determined if sn(u) is computed.

2.1.3 Closed Form Solution for Force-Separation Relation

As seen in the previous section the force-separation relation involves several complicated functions which can be computed only numerically. A closed form solution is required to gain a physical insight into the influence of geometrical and structural parameters involved. This step requires some approximations and the analysis is as follows.

$$\delta/2 = x - (d/2)\sin\theta \tag{2.22}$$

For small deflection angle (small α), angle of rotation θ also small. After examining the numerical results for different cases it was found that the value of x remains close to x_0 . Using the half angle formula and the condition of small θ ,

$$\sin\theta \sim 2\sin(\theta/2)$$
 (2.23)

This implies
$$\delta/2 \sim x_0 - d\sin(\theta/2) \tag{2.24}$$

Substituting for θ in terms of the Jacobian elliptic sine function and terminal deflection angle results in

$$\delta/2 \sim x_0 - d \, p \, sn(u, p) \tag{2.25}$$

p is related to force through the complete elliptic integral of first kind. u has a direct relation with the force. Therefore, it is now required to invert the elliptic integral of first kind to get a relation between p and force and to express the elliptic sine function as a Taylor series expansion in terms of u and p so as to obtain the final expression in terms of force. In the limit of small p which is true for small deflection angle, the complete elliptic integral can be expressed as

$$K(p) \sim (\pi/2)(1 + (p/4) + (9p^2/64)..)$$
 (2.26)

Higher order terms apart from the linear terms can be neglected resulting in

$$p \sim (8/\pi)(\sqrt{F/EI})l - 4$$
 (2.27)

It is well known that the Jacobian elliptic sine function tends to a normal sine function for small values of p. That is

$$sn(u,p) \to \sin(u)$$
 (2.28)

But since the linear terms in p are retained, a Taylor series expansion of the Jacobian elliptic sine function is required to make the right approximation in the limit of retaining terms linear in p. The expansion reported in [25] has no terms linear in p, therefore, neglecting all the higher order terms results in equation 2.28. Using equations 2.27 and 2.28 in 2.25 results in the expression

$$\delta/2 \sim x_0 - d \left[(8/\pi)(\sqrt{F/EI})l - 4 \right] \sin(u) \tag{2.29}$$

From equation 2.20,

$$u = K(p)(x_0/l) \tag{2.30}$$

and from equations 2.10 and 2.12,

$$K(p)/l = \sqrt{F/EI} \to u = \sqrt{F/EI} x_0 \tag{2.31}$$

Therefore, the final closed form expression relating separation and force is given by

$$\delta \sim \delta_0 - 2d \left[(8/\pi)(\sqrt{F/EI})l - 4 \right] \sin\left(\sqrt{F/EI}(\delta_0/2)\right) \tag{2.32}$$

2.1.4 Incorporation of Surface Effects for Small Deflection Angles

From equation 2.8, the force term in the integrand can be approximated for small deflection angles as follows

$$F(\cos\theta - \cos\alpha) - (d/2) \tau D(\cos 2\theta - \cos 2\alpha) \rightarrow [F - (2\tau^{0}D)](\theta^{2} - \alpha^{2})/2$$

$$(2.33)$$

which implies in the limit of zero α equation 2.16 gives

$$F = F_{cr} = (\pi^2 (EI)^* / 4l^2) + 2\tau D \tag{2.34}$$

This is the same result predicted in [11] for critical force using a different approach which cannot accommodate the analysis for determining the separation change under the action of forces greater than the critical value. Following equations 2.8 and 2.33 it is immediately seen that the effect of residual surface tension and surface elasticity can be incorporated in the closed form expression in the following manner

$$\delta \sim \delta_0 - 2d \left[(8/\pi) (\sqrt{(F - 2\tau D)/(EI)^*}) l - 4 \right] sin \left(\sqrt{(F - 2\tau D)/(EI)^*} \, \delta_0 / 2 \right)$$
(2.35)

2.2 Tunneling Current

The tunneling current through the structure considered would be through the least action path i.e. the maximum probability path [26-28]. Therefore, the actual width of the barrier seen by the electron would correspond to the distance between the lower edges of the nanoparticles which is the least distance between the metallic regions at the center. From the results of elemental detection experiments (Chapter 4) it was identified that the segmented structure was composed of metallic nanoparticles embedded within an insulating medium. Hence, the tunneling current is determined using a Metal-Insulator-Metal (MIM) model. Only the important details of the model are presented here.

2.2.1 MIM Model

Penetration of a quantum wave through a barrier of finite height and width is referred to as tunneling [29]. This is a purely quantum mechanical phenomenon with no classical counterpart. If two metallic regions were separated by a sufficiently thin insulating region, current would flow through the junction due to tunneling effect. A model of this system for a wide voltage range was first developed by Simmons [30]. Equilibrium condition requires the invariance of the Fermi level across the junction. This places the conduction band edge of the insulator above the Fermi level of the metal introducing an effective barrier for the flow of electrons. Current flow across the junction can occur if the electrons have sufficient thermal energy to surmount the barrier or if the barrier is thin enough to enable penetration by the tunneling phenomenon. The temperature of the system is assumed to be low enough to neglect thermal effect and to consider current contributions only due to tunneling. According to the Wentzel-Kramer-Brillouin (WKB)

semi-classical approximation the probability of transmission of an electron wave with energy E through a barrier V(x) (1-D potential dependent on the position) is given by

$$T(E) = \exp\left(-2\int_{a}^{b} \sqrt{4\pi m(V(x) - E)/h}\right)$$
 (2.36)

where a and b are the semi-classical turning points and the energy is the energy of the quantum particle in a direction perpendicular to the 1-D barrier, m is the mass of the quantum particle and h is Planck's constant. The potential profile of the system at equilibrium is schematically illustrated in figure 2.7.

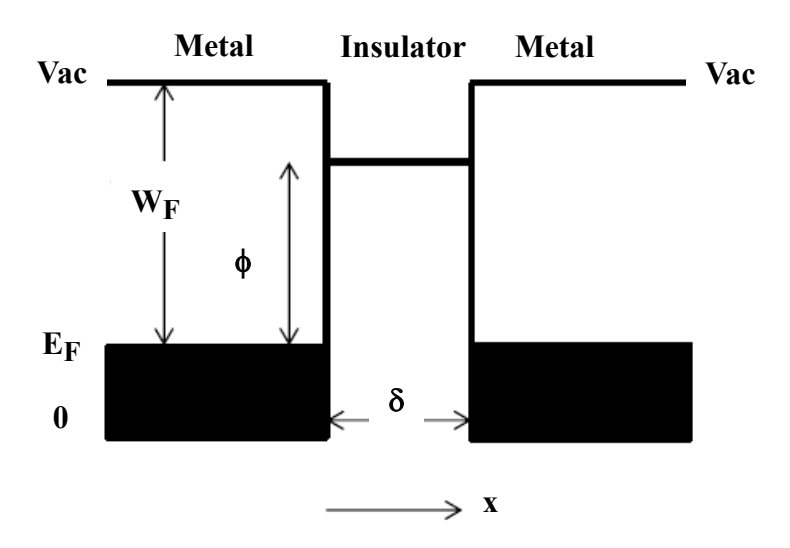


Figure 2.7 Equilibrium potential profile of the junction. E_F is the Fermi energy of the metal, W_F is its work function and ϕ is the equilibrium barrier height as seen by the electrons in the metal.

A free electron model is adopted for the metal electrodes wherein the E-k relation is an isotropic distribution (where k is the wavenumber of the electron). Under application of voltage, equilibrium is disturbed and the potential profile across the junction depends on the magnitude of the voltage.

Following [30], the generalized expression for tunneling current is given by

$$I = I_0 \left[\bar{\phi} \exp \left(-C\sqrt{\bar{\phi}} \right) - (\bar{\phi} + eV) \exp \left(-C\sqrt{\bar{\phi} + eV} \right) \right] \tag{2.37}$$

where $\bar{\phi}$ and Δx are the average barrier height and the effective barrier width as seen by the tunneling particle.

2.3 Sensitivity of the Force Sensor

Following [9], the sensitivity of a force sensor can be defined as the differential change in current for a differential change in force. For the sensor under consideration this value would be different for different regions of operation due to the non-linear current-force relation which is expected. Therefore, the sensitivity value would be of critical importance to decide the regime of operation for a particular application.

Chapter 3

Numerical Results

In the last chapter separate mechanical and electrical models were developed to study independently the effect of external buckling force on the lower edge separation and the dependence of the tunneling current on the barrier separation. In this chapter the two models are combined to theoretically study the force-current relation and to compute the corresponding sensitivity values needed to characterize the sensor. In the first part of this chapter changes in the lower edge separation for different force values are numerically obtained followed by calculating the current for the corresponding changes. Variations in the structural dimensions and mechanical properties of the external nanowire and the pods are considered and the related effects on the force-separation relation, force-current relation and the sensitivity are compared.

3.1 Effect of Force on Separation

In this section the effect of external buckling force on the separation between the lower edges of the center pods is studied. Since both the external force and the separation are determined by the terminal angle α , we can use this as an intermediate variable to correlate the change of separation with force. This relation is plotted in figure 3.1. Following are the parameters considered for this simulation: E = 100 Gpa, D = 20 nm, d = 7.5 nm, L = 800 nm and $x_0 = 0.5$ nm. The symbols used for the parameters are as followed in the previous chapter. The forces were computed using α values from five to eighty degrees. The upper limit of 80^0 was chosen for the simulation to verify if the trend would be non-linear even for the small to intermediate deflection range. There are some interesting features that can be understood from the force-separation curve.

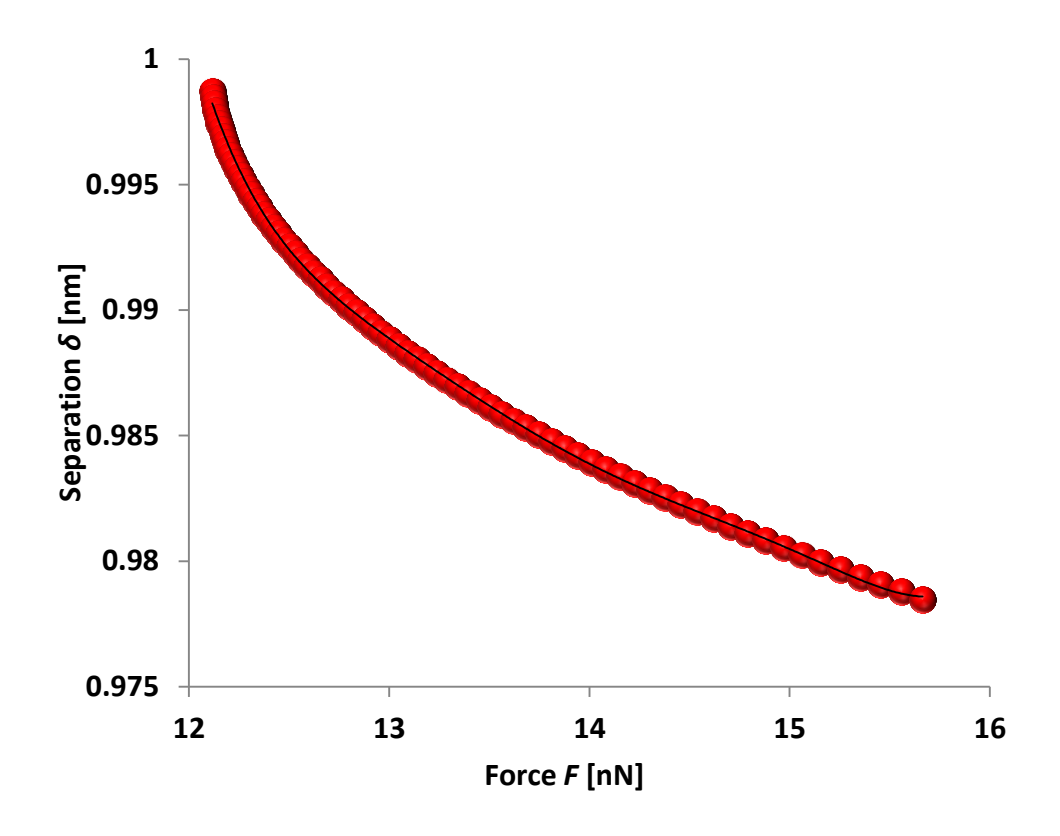


Figure 3.1 Force-Separation (F- δ) curve. Here, the Young's modulus is 100 GPa, the diameter of the nanowire is 20 nm, the diameter of the pod is 7.5 nm, length of the nanowire is 800 nm. The F- δ curve can be fitted using a fourth degree polynomial which is as a result of the complex relations involved in the formalism related to elliptic integrals. However, the non-linearity can be easily understood from the closed form expression (equation 2.47) which approximately relates δ as function of \sqrt{F} . This is a remarkable feature of the structure because the separation decreases non-linearly with force establishing an important feature of the device structure: small increase in force around the point of buckling is sufficient to produce significant reduction in separation which in turn would cause a significant enhancement in the tunneling current. The desired feature of the device that was predicted would therefore be observed. Numerical results confirming this are presented in the following sections. From figure 3.1 it can be observed that the greatest reduction in the separation occurs for the initial forces applied. This region is the

region of non-linear change which for the model parameters considered is from around 12nN to 12.5nN. Beyond this the change appears to be almost linear i.e. a quasi linear decline. The overall reduction in the separation for the force range considered is found to be ~ 2% (from 1nm to about 0.98nm). Though this appears to be a very small change when compared to the force range (12-16nN) this would have an appreciable effect on the tunneling current due to the exponential dependence of the tunneling phenomenon on the separation.

3.2 Effect of Separation Change on the Tunneling Current

Based on the MIM model the relation between the tunneling current and the junction width was expressed in equation 2.54. Since only structural enhancement to the tunneling current is considered, small voltage condition is assumed and if only changes in the separation between the lower edges of the center pods are significant, the tunneling current through the structure could be approximated as a function of the separation as shown

$$I(\delta) \to I_0 \exp\left(-\left(4\pi\delta\sqrt{2m\phi_0}\right)/h\right)$$
 (3.1)

3.3 Effect of Buckling Force on the Tunneling Current – A Combined Model

The effect of buckling force on the tunneling current was obtained by computing the current values for different separation values which are related to the force using the relation illustrated in figure 3.1. A plot showing the current-force variation is displayed in fig 3.2. The same model parameters were used to obtain the plot.

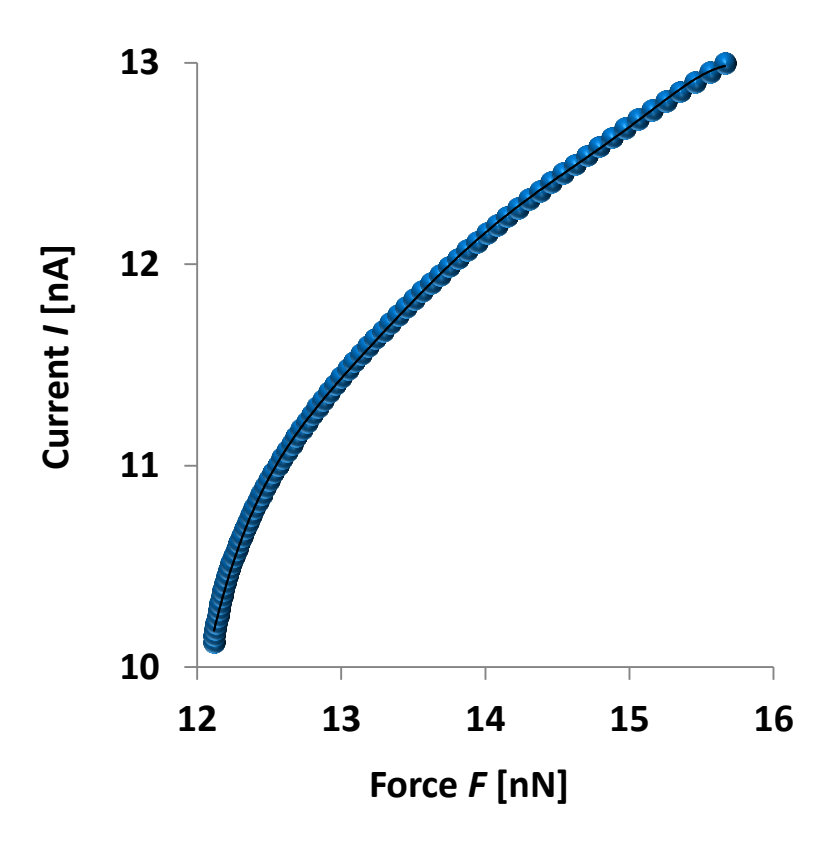


Figure 3.2 External force induced enhancement in tunneling current.

The desired non-linear increase in current w.r.t. force is observed. The initial force range causes a sharp rise in current and as the force increases to larger values i.e. for larger values of the terminal deflection angle the current change is observed to be quasi-linear. The current increases from 10.2nA to 11nA for an increase in the force value from 12.2nN to 12.5nN implying a rise of about 3nA for every nN increase in force value. However, in the linear regime there is a rise of only 0.67nN for every nN rise in force. The trend suggests that for the device structure to be sensitive to very small changes in the force it must be operated in the non-linear regime while for greater range of force measurements, operation in the linear regime would be preferred.

3.4 Sensitivity Curve

Using the definition for sensitivity as defined in the previous chapter a sensitivity plot was obtained (figure 3.3). The current and force values used for this calculation were adopted from the previous section.

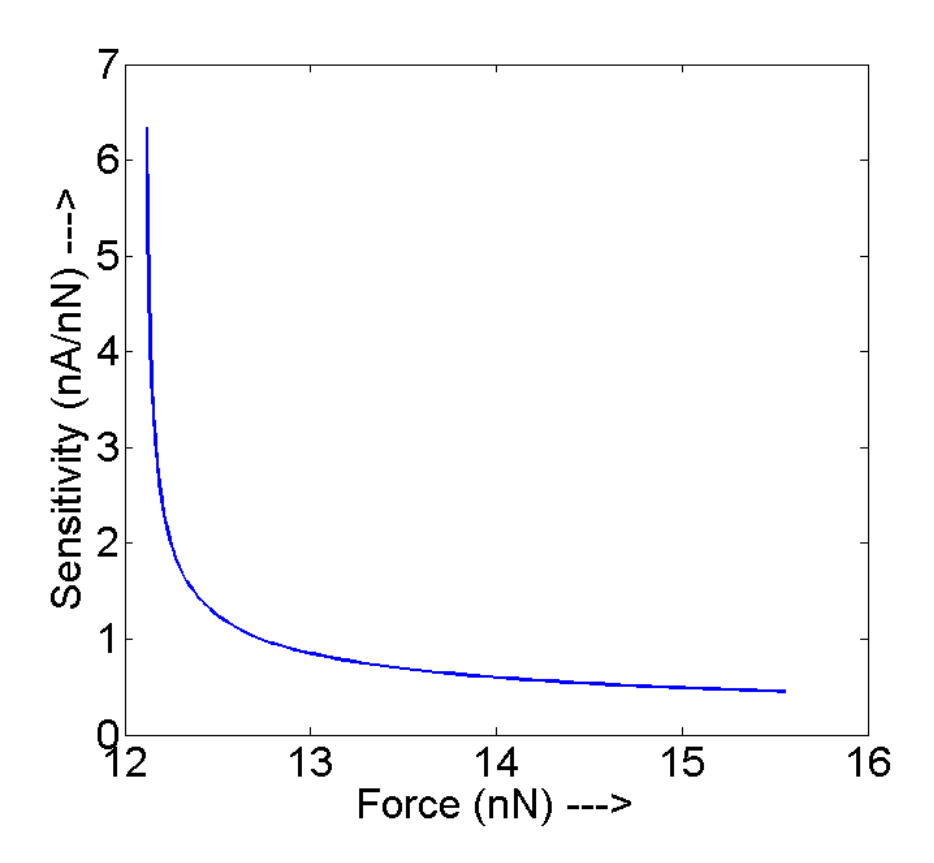


Figure 3.3 Sensitivity values for the force range considered.

From figure 3.3, sensitivity as high as 6.5nA/nN is shown be to theoretically possible for small changes in the force. Compared to the values reported in [9] this is a tremendous improvement affirming the highly sensitive nature of the device structure. Though the overall trend is non-linear, the device could be operated within a specific range of force values where the variation could be approximated as linear and the high sensitivity could be made use of. In the following section other variations are considered and their effects on the force-separation and force-current relations are discussed.

3.5 Dimensional Variations: Effect of Length, Outer and Inner Diameter

If the length of the nanowire considered for the simulation was reduced to one-fourth of its initial value (200nm) with other parameters similar to those used to obtain the plot in figure 3.1, the force-separation relation is as shown in figure 3.4.

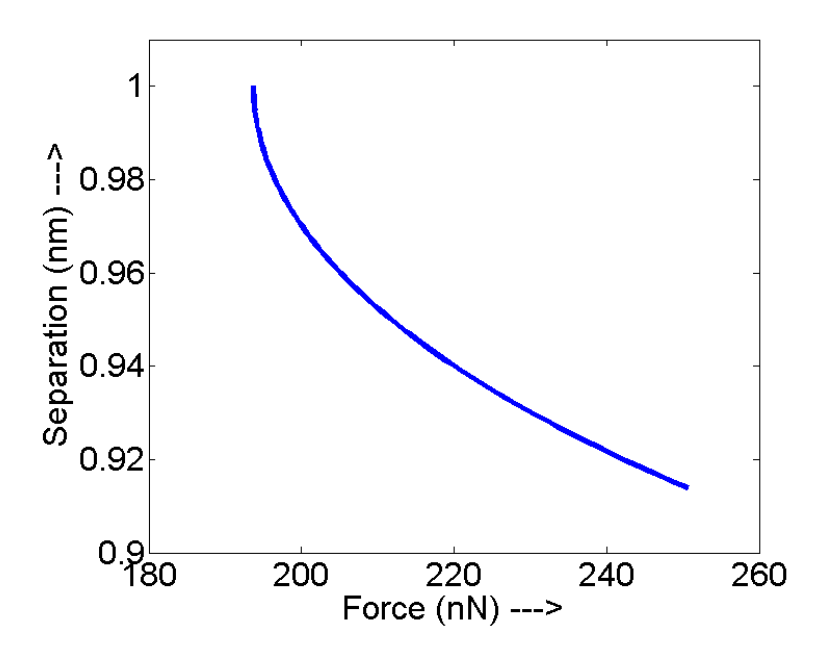


Figure 3.4 A greater drop in separation along with shifted and increased force range is observed for smaller length.

This effect due to smaller length can be understood from the closed form expression relating force and separation. The shift in force and increase in force range can be understood from the expression for critical force (equation 2.49 without surface effects) which depends on the inverse square of length. From the sinusoidal term it is clear that for forces above the critical force, the ratio of initial pod separation to the length of the wire decides the extent of drop (the ratio can be interpreted as a frequency term). Since the initial separation cannot be increased above the sub-nm range (effects of tunneling would not be pronounced), to maximize the decrease in separation an optimum length could be chosen. The effect of varying the diameter of the pod is better

understood if its mechanical property is also incorporated in the model. This is done by modifying the flexural rigidity (equation 2.3) into a composite rigidity.



Figure 3.5 Cross section of the device structure with outer diameter D and inner diameter d and Young's modulus E_1 and E_2 respectively.

The cross section of the device is as shown in figure 3.5. For a symmetric structure considered, the combined flexural rigidity takes the form

$$(EI)_c = E_1 I_1 + E_2 I_2 (3.2)$$

 E_1 and E_2 are the Young's modulus of the outer shell and the inner pod and I_1 and I_2 are their corresponding area moment of inertia. This modification in the flexural rigidity would have an effect on the force values computed. To illustrate this effect the Young's modulus of the inner pod is taken to be 50GPa for simulating the force-separation relations for a fixed outer diameter and varying inner diameter and the corresponding current-force relations for a fixed voltage of 0.2V and equilibrium barrier height of 1eV. The other parameters are similar to the ones employed for obtaining plots in figures 3.2-3.4. For terminal deflection angles from zero to eighty degrees, the force-separation and force-current density relations for inner diameters 8nm, 7.5nm and 7nm are plotted in figure 3.6. The interesting cross over regions observed are analyzed in terms of the influence of the inner diameter on the critical force.

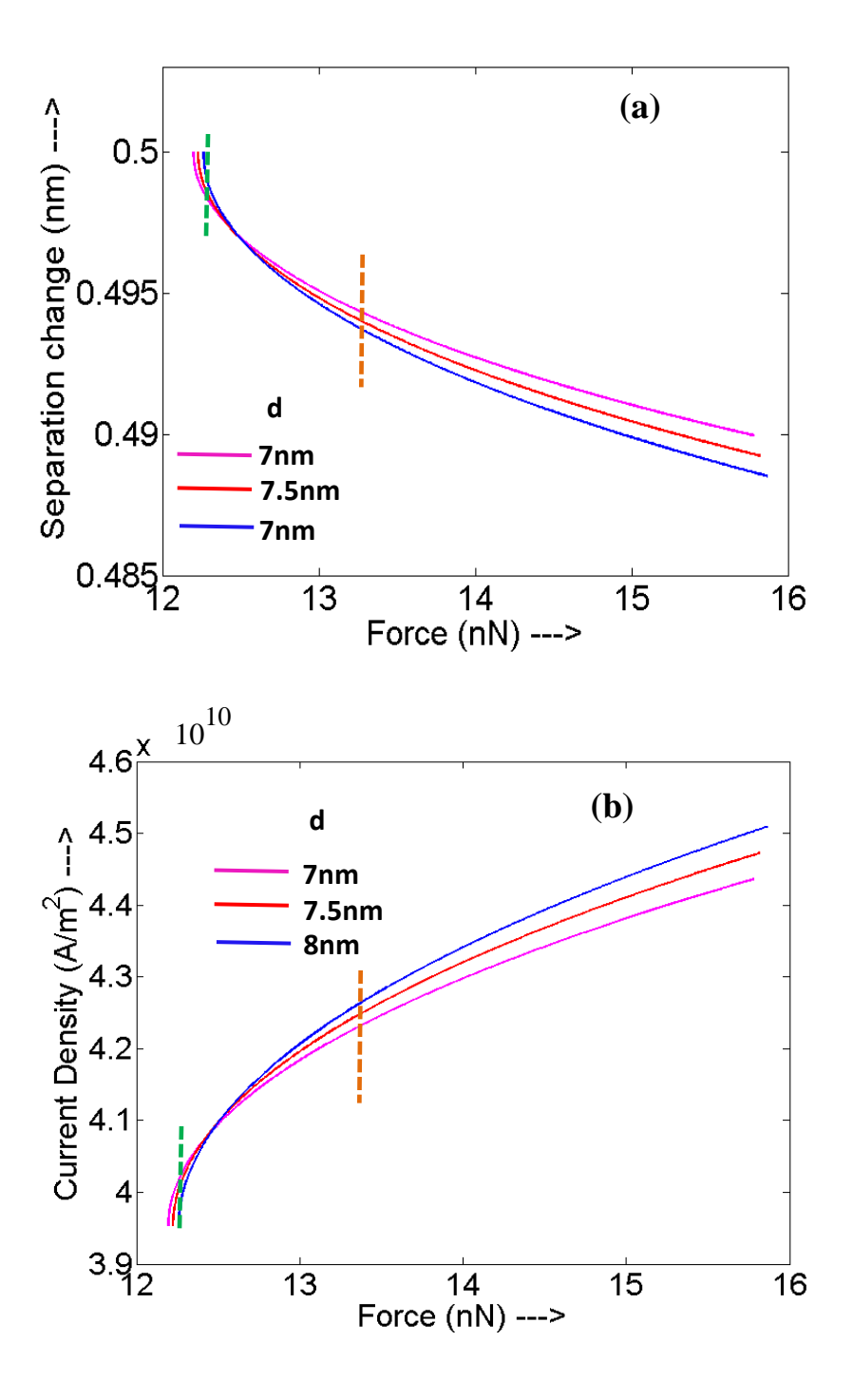


Figure 3.6 a) Relation between force and separation change and b) relation between force and current density for inner diameters 8nm (blue), 7.5nm (red) and 7nm (pink) are plotted for α values from five to eighty degrees. Outer diameter fixed at 20nm.

From figure 3.6a, it is noted that the structure with smaller inner diameter corresponds to a smaller critical force which is quite obvious from the equation relating force and the flexural rigidity. However, the interesting feature is the greater drop in the separation for the structure with smaller inner diameter till the point of cross over (along the dashed green line in figure 3.6a) while beyond this point the separation change is greater for the bigger inner diameter structure (along the dashed yellow line in figure 3.6a). This has a corresponding effect on the current density calculated. As seen in figure 3.6b the rate of increase in current density w.r.t. force is greater for the structure with smaller inner diameter (along the dashed green line in figure 3.6b) while beyond the cross over region the bigger diameter structure causes a greater rise in current density w.r.t. force (along the dashed yellow line in figure 3.6b). The maximum current density values calculated for the maximum α considered are 4.436 x10¹⁰ and 4.472 x10¹⁰ and 4.51 x10¹⁰ A/m² respectively. The subsequent change in the maximum current density value for every 0.5nm increase in the inner diameter is found to be 0.82%.

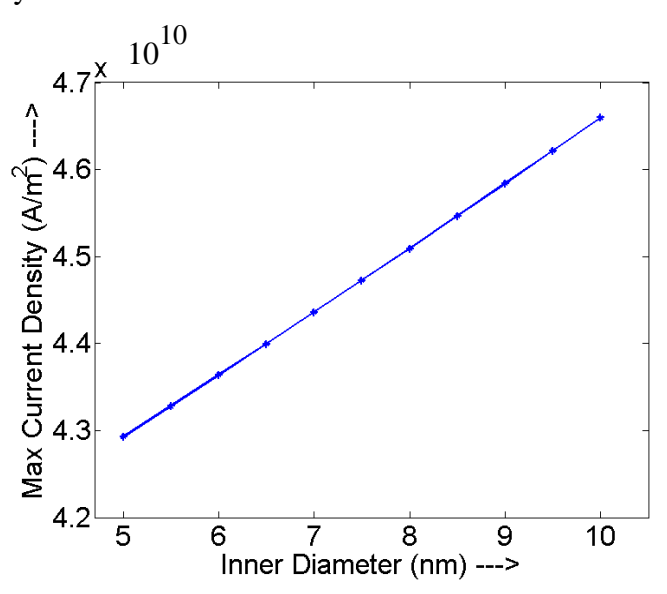


Figure 3.7 Relation between the maximum current density and the inner diameter.

This constant value suggests that the maximum current density would scale linearly with the inner diameter. This is confirmed by the plot in figure 3.7 implying the simple conclusion that to maximize the maximum current density achievable the inner diameter has to be increased.

Though the interesting cross over regions are observed in the force-separation and force-current density plots, the sensitivity plot for different inner diameters and constant outer diameter shows no such cross over regions. Sensitivity in this case is defined w.r.t. current density. An affirmative conclusion that the structure with greater inner diameter enhances the sensitivity can be reached. However, if the ratio of outer diameter to inner diameter is kept fixed and if each is varied accordingly an opposite effect is observed.

Chapter 4

High Resolution Imaging and Elemental Detection

This chapter presents the technique used for high resolution imaging and elemental detection of a segmented nanowire of interest. It begins with the introduction of High Resolution Transmission Electron Microscopy (HRTEM) which is employed for obtaining high resolution images of the segmented nanowire. The high resolution images obtained are then presented. This is followed by the introduction of X-ray Energy Dispersive Spectroscopy (XEDS) for elemental detection. The results obtained for the nanowire of interest are then presented followed by a discussion of the demerits of this method and the need for an advanced technique. A brief introduction of the Electron Energy Loss Spectroscopy (EELS) and elemental mapping using the Energy Filtered Imaging technique are then presented. Results obtained by each method are then compared. Finally, a possible method for further improving the analysis is described. The introductory contents of the sections till section 4.2.2 are based on [31] while those of the subsequent sections are based on [31, 32]. All the results presented in this chapter were obtained using a JEOL 2200FS Transmission Electron Microscope equipped with the necessary instruments for performing X-EDS and EELS analysis and imaging using HRTEM, STEM and EFTEM mode.

4.1 High Resolution Transmission Electron Microscopy (HRTEM)

Transmission Electron Microscopy has become an important tool for investigating the structure and composition of nano-scale materials due to the advantages it offers in terms of high spatial and analytical resolution. HRTEM is a powerful technique used for studying structures of interest 'locally' i.e. on the atomic scale. The scattering of the electron beam by the sample causes a change in the amplitude and phase of the incident beam. This change results in the

contrast observed in TEM images. Different kinds of contrast are possible in the TEM. Amplitude contrast is due to the variation in the mass, thickness or the atomic weight of the sample constituents. Diffraction contrast is due to the crystal orientation difference or defects while phase contrast is due to the electron interference as a result of phase difference. Figure 4.1 shows the schematic of image formation by amplitude contrast.

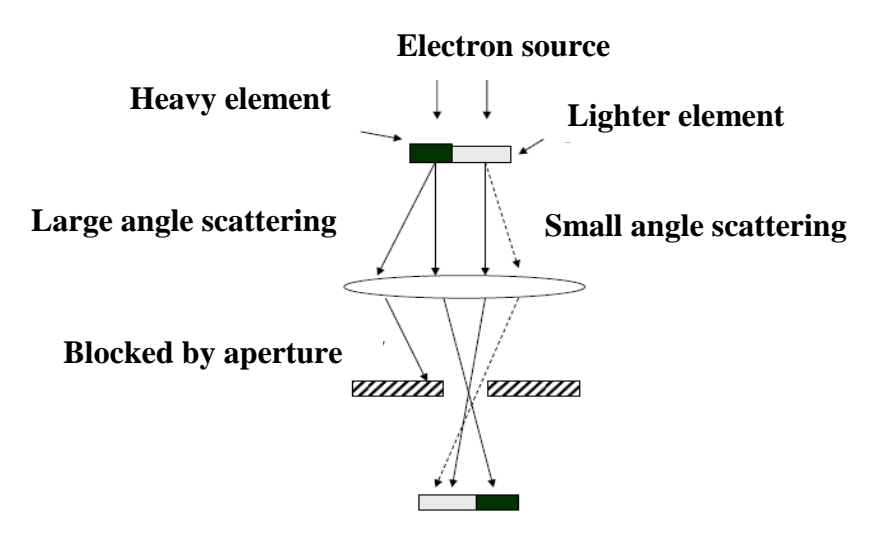


Figure 4.1 Schematic of image formation by atomic number contrast and mass-thickness contrast.

Two kinds of images, a Bright Field (BF) image and a Dark Field (DF) image can be obtained using the TEM. BF image uses the forward scattered electrons while the DF image uses diffracted electrons. However, a HRTEM image is a phase contrast image. While the BF and DF image can be formed by selecting a single beam, a phase contrast image requires a collection of beams for the image formation.

4.1.1 Weak Phase Object Approximation (WPOA)

Phase contrast image formation can be explained using WPOA. The incident electron beam on interaction with the specimen acquires a phase shift. This interaction occurs due to the

electrostatic potential of the specimen atoms. If the mean electrostatic potential (projected) is denoted by ϕ_0 and the interaction strength by σ then the phase shift acquired by the incident electron beam is given by

$$\Psi_{\rho}(x,y) = \exp(-i\sigma\phi_0(x,y))\Psi_0(x,y) \tag{4.1}$$

where $\Psi_0(x,y)$ and $\Psi_e(x,y)$ are the wave functions of the incident and transmitted electron beams respectively and $\exp(-i\sigma\varphi_0(x,y))$ is the referred to as the specimen transfer function. This linear relationship between the incident and transmitted electron beams through the projected electrostatic potential of the specimen is called the WPOA. It is important to note that this approximation holds only for very thin samples composed of light elements.

4.1.2 Phase Contrast from the Lens

The ability of a lens to pass the electrons after interacting with the sample is governed by the contrast transfer function T(u) given by

$$T(u) = 2A(u)sin\chi(u)$$
 (4.2)

where u refers to the reciprocal space lattice vector, A(u) is the aperture function and $\chi(u)$ is the phase distortion function, which is a function of the spherical aberration C_s , defocus Δf and electron wavelength λ . The first zero point of T(u) corresponds to the best resolution and allows the direct interpretation of bright/dark contrast as atom position. This point is called the Scherzer resolution and is achieved when the transfer function is optimized by balancing the effect of spherical aberration at a certain negative value of defocus referred to as Scherzer defocus.

This defocus condition causes the electron at different reciprocal lattice positions to be transmitted in nearly constant manner i.e. similar phase and amplitude up to the Scherzer resolution limit also referred to as the information limit as shown in figure 4.2b.

It is possible to acquire images of structures with features below this limit by passing the higher reciprocal space frequencies. But the image interpretation becomes difficult because not all the information is passed in the same manner. This can be understood from figure 4.2 which displays the contrast transfer function and the phase distortion function as a function of the reciprocal space lattice vector.

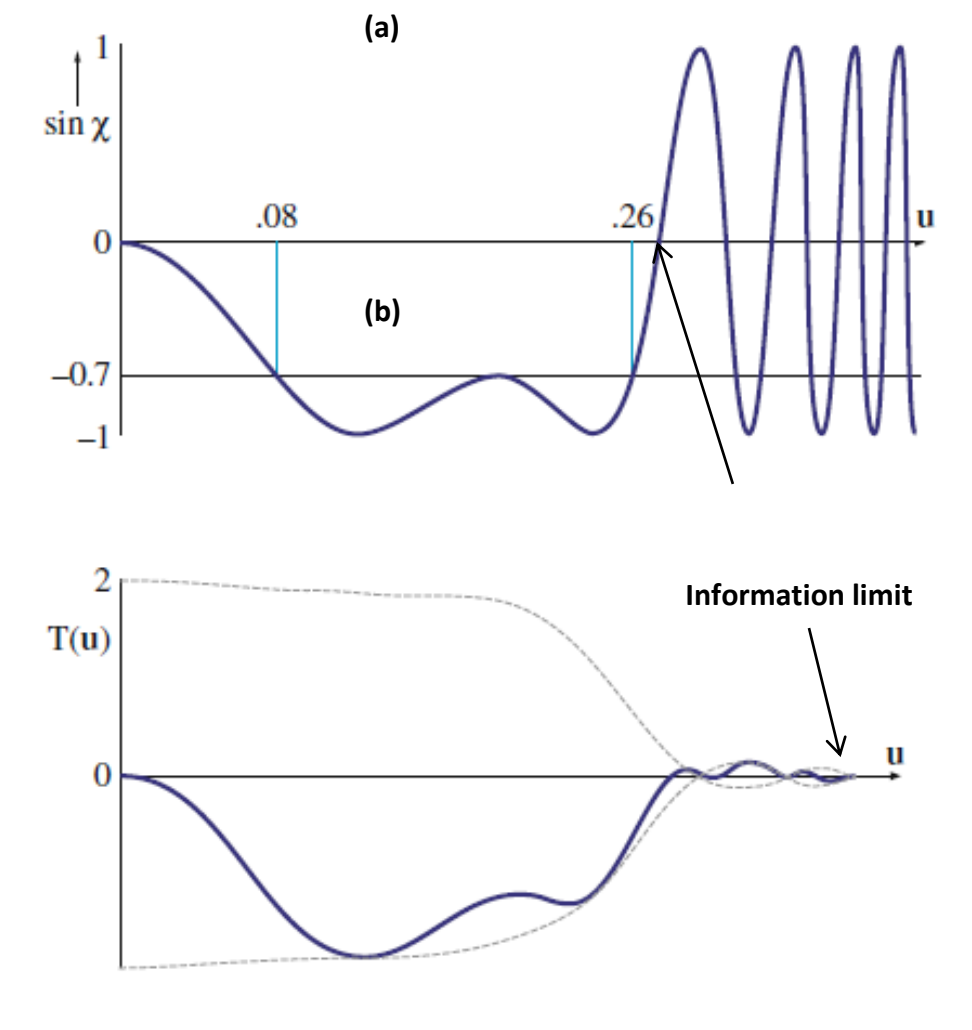


Figure 4.2 (a) Phase distortion function vs. u and (b) Contrast transfer function vs. u [31].

Having described the essential aspects of HRTEM, some of the high resolution images of the heterostructured nanowire are presented in figure 4.3.

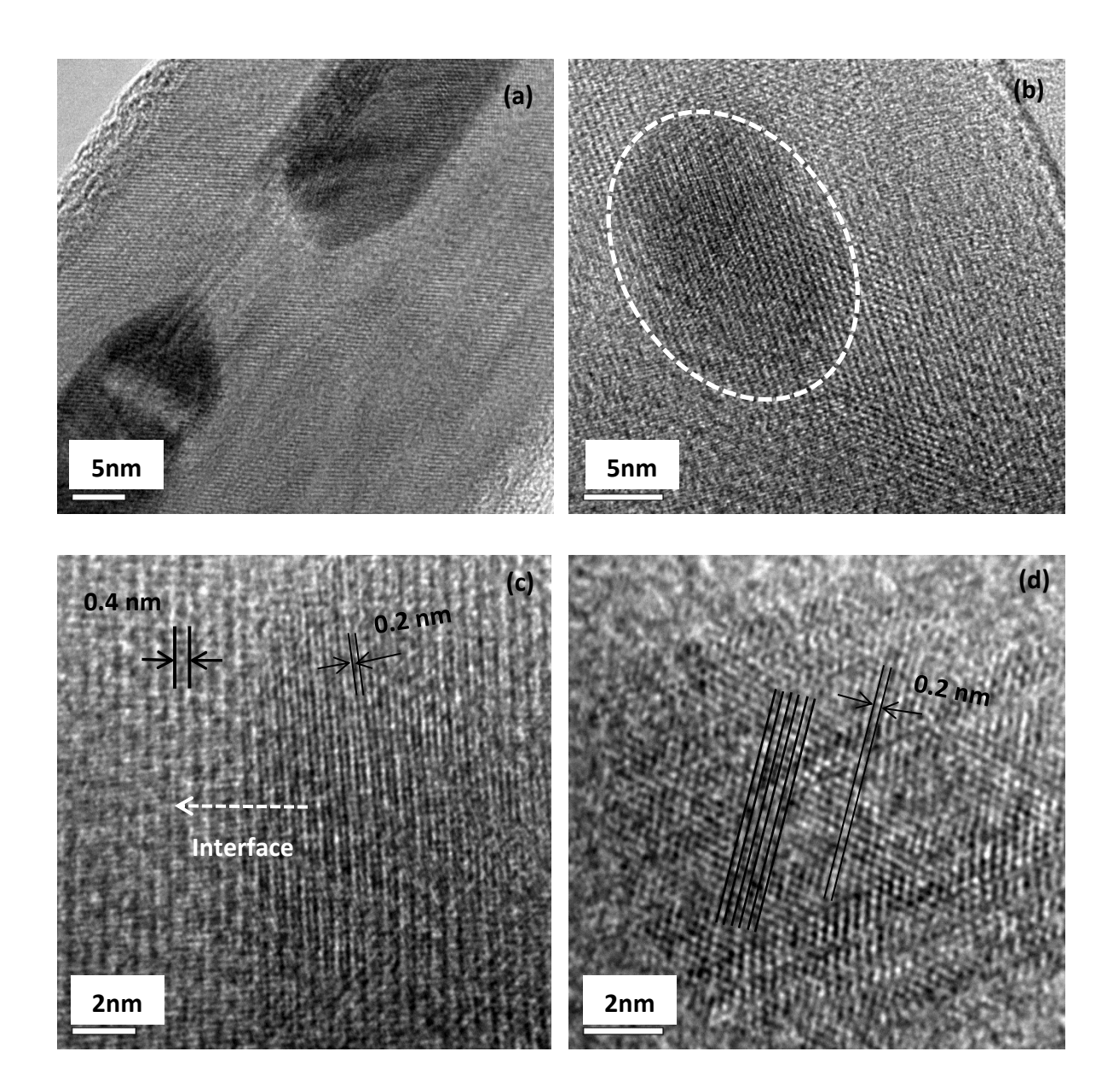


Figure 4.3 HRTEM images of a section of the heterostructured nanowire at magnification (a) 600K (b) 800K (c) 1.2M (d) 1.5M. Lattice fringes are observed in every image.

All the images clearly display the lattice fringes indicative of the crystal structure for the embedded particle and the external nanowire. Figure 4.3c shows the magnified view of the interface between the embedded nanoparticle and the external nanowire. The lattice fringes corresponding to the two regions seem to be aligned suggesting that the growth direction for both structures could be similar. Figure 4.3d shows the image of the embedded nanoparticle magnified by about a million times. The atomic lattice fringes are quite aligned suggesting that the structure could be a single crystal.

4.2 Elemental Detection: X-EDS, STEM-XEDS, EELS, EFTEM

Inelastic scattering of electrons on interaction with the sample generates a whole range of signals which can give useful information about the chemistry of the sample than that which can be understood from the elastic electrons. On undergoing the inelastic scattering, in addition to the electrons with energy loss other signals like characteristic X-rays, secondary electrons and visible light are also generated. Modern TEMs are equipped with the detector to collect the signals and with the advancements in the spatial resolution and the detection limit of the various techniques it has become possible to well characterize nanostructured materials. For this it is important to understand the origin of these signals, the collection methods and how they could be interpreted for compositional analysis. When a high energy electron encounters an atom of the nucleus it first interacts with the outer loosely bound electron cloud and then penetrates the tightly bound inner core shell electrons and the finally may interact with the nucleus. This range of inelastic scattering produces a range of scattering angles. However, there is no simple relationship between the energy lost and the scattering angle. In general, the greater the penetration of the electron into the atom the greater is the energy loss. The inelastic scattering

can be classified into processes that generate X-rays and processes that generate secondary electrons.

4.2.1 X-ray Energy Dispersive Spectroscopy (X-EDS)

X-ray is one of the most important secondary signal generated by the electron beam's interaction with the sample. Analyzing the X-rays gives a quick glimpse of the elements that constitute the sample. It is also possible to quantify the amount of element present in the sample. The X-rays produced in the TEM are of two kinds – the Characteristic X-rays and the Bremsstrahlung Xrays. The characteristic X-rays are useful for local elemental analysis hence of particular advantage for analysis of nanostructured materials and crystal defects. The Bremsstrahlung Xrays are considered a disturbance for material analysis while are useful for biologists. Since the characteristic X-rays are of greater importance, more details on their generation and usefulness are presented. When a high energy electron penetrates through the outer (conduction) shell electrons and interacts with inner (core) shell electrons and if the energy transferred to the inner shell electron is high enough to let the electron escape from the coulomb field of the nucleus, the core electron escapes leaving an empty state (hole) in the inner shell. This causes the ionization of the atom and is elevated to an excited state. The ionized atom can be lowered to its ground state energy when an electron from an outer shell falls into the empty state. This transition of an higher energy outer electron to a lower energy state is accompanied by the emission of a X-ray or an Auger electron. In both cases the emission is characteristic of the difference in energy between the two levels involved and since this difference is unique to an atom, the corresponding X-ray emission is termed as a Characteristic X-ray emission. A schematic of the X-ray generation is shown in figure 4.4. X-rays are also generated by processes other than electron beam bombardment. The different characteristic X-rays are identified with the different electron shells. The innermost electron shell is called the K-shell, the next is called the M-shell and so on. All the shells except for K shell also have subshells, for example L_1 , L_2 etc.

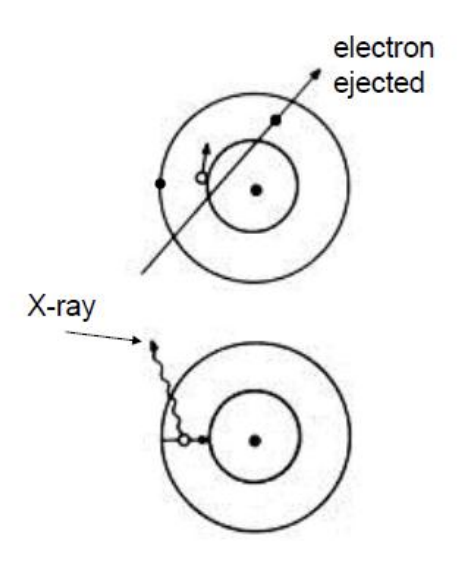
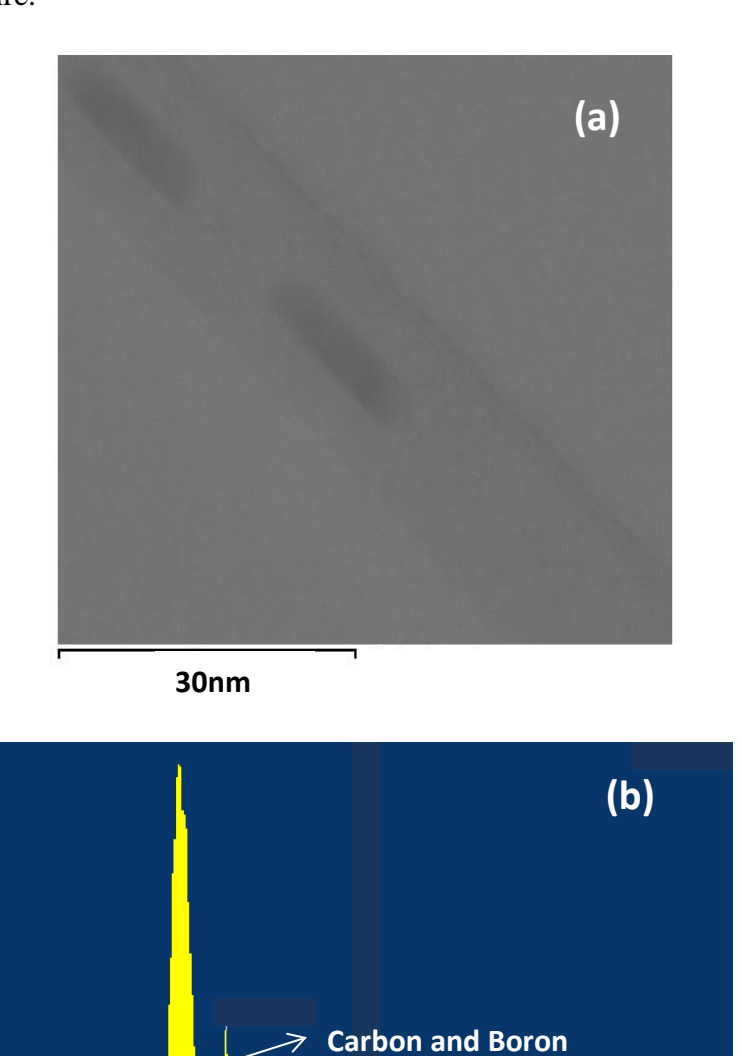


Figure 4.4 Schematic of the characteristic X-ray emission.

A characteristic X-ray is labeled based on the shell being filled and the shell from which the electron comes. If a K shell hole is filled from a L shell the corresponding X-ray emitted is called the K_{α} X-ray. In the spectrum collected, the X-ray emissions appear as characteristic X-ray peaks.

A brief overview of the spectrum collection could be instructive. The X-rays generated from the sample are collected using a commercial spectrometer referred to as the X-ray Energy Dispersive Spectrometer (X-EDS). The spectrometer consists of a Si semiconductor detector which generates voltage pulses that are proportional to the X-ray energy. Electronic processing of the signal transforms the X-ray energy into a signal in a specific channel in a computer controlled storage system. The counts in the energy channels are then displayed as a spectrum. Figure 4.5

displays the X-ray Energy Dispersive Spectrum along with the high magnification picture of the hetero-structured nanowire.



peak merged

1.4

Nickel peak

1.8

KeV

Figure 4.5 (a) A high magnification picture of the heterostructured nanowire and (b) X-ray EDS obtained from the corresponding region.

0.8

0.4

-0.2

From the spectrum it can be understood that the region contains Nickel and Carbon. However, an appreciable overlap of the Carbon peak with Boron makes it difficult to affirmatively confirm the if Boron is present or absent. This overlap is due to the small difference in the energy values corresponding to the characteristic peaks of Boron and Carbon and the low Boron count in comparison to Carbon count. In order to confirm the presence or absence of Boron and to spatially resolve the elements detected, a more powerful technique involving X-EDS using a Scanning Transmission Electron Microscope (STEM) was adopted.

4.2.2 Scanning Transmission Electron Microscopy (STEM):

A Scanning Transmission Electron Microscope (STEM) is the operation of the TEM in the scanning mode. Instead of a parallel illumination the beam is converged to a spot probe which scans along the specimen. Beam scanning is controlled by the scan coils and not by any lens. Figure 4.6 shows the bright and dark field images of the heterostructured nanowire. Advantage of the type of the image is specific to the purpose and the sample.

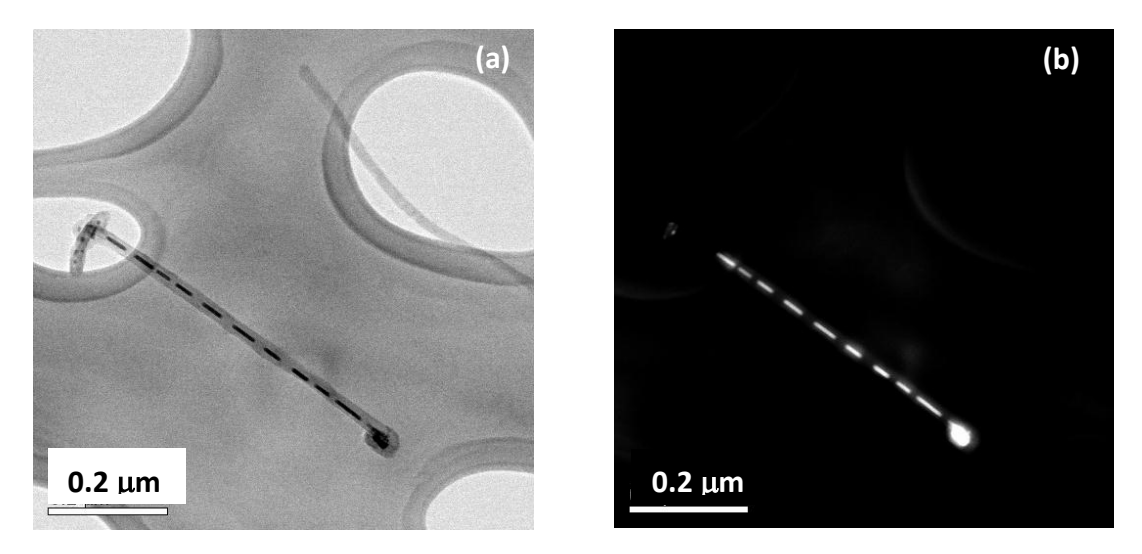


Figure 4.6 (a) Bright Field (BF) STEM image and (b) Dark Field (DF) STEM image of the heterostructured nanowire.

An interesting observation from figure 4.6 is that the nanowire without any embedded nanoparticles is visible in the bright field image while it is absent in the dark field image. This could be due to the limited scattering from the low atomic number region when compared to the dark (heavy atomic number) region, since the images are formed by collecting the electrons scattered by the respective regions of the sample. STEM-XEDS can be carried out in spot mode, line scan mode or area scan mode. Spot mode involves stopping the beam scan and acquiring the spectrum from a particular spot of interest. A variation of the spot mode is the line scan mode which involves acquiring spectrum from many spots along a linear feature of the sample. By this technique elemental profile along a line can be obtained which could provide useful insights about the variation of the composition across an interface. Figure 4.7 presents the line scan results from a region of the heterostructured nanowire along with the corresponsing X-EDS. Excellent profile for the element Nickel is obtained, however, the profile corresponding to Boron and Carbon show no such distinct variation. For analyzing the variation of Nickel concentration across the inter-nanoparticle separation a line scan was performed across the gap on a different region of the nanowire. The results are shown in figure 4.8. A clear decline in the Nickel concentration along the gap is observed with the darker particle corresponding to greater concentration demonstrating the simple and obvious aspect of X-ray generation being proportional to the elemental concentration.

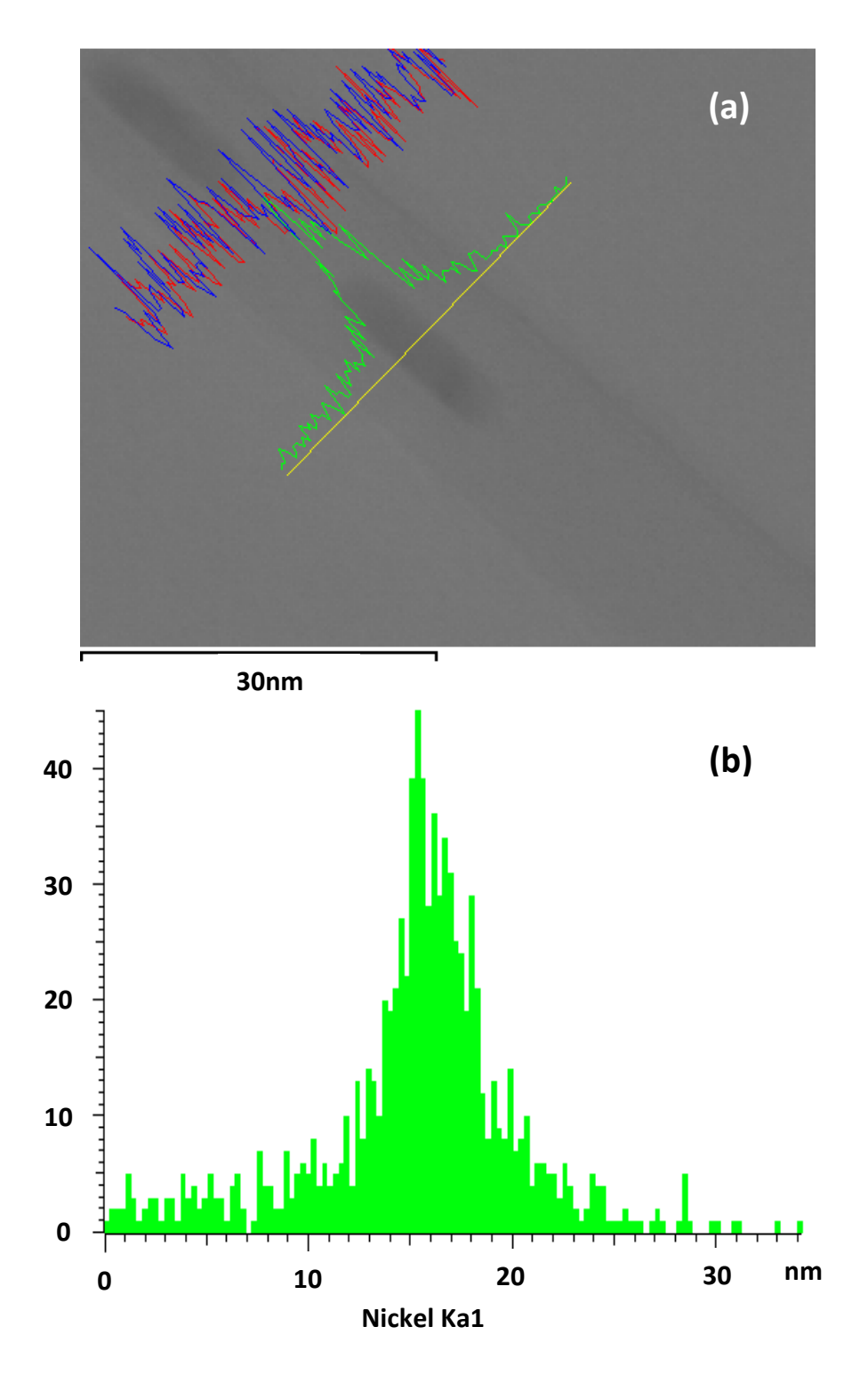


Figure 4.7 (a) Image of a section of the heterostructured nanowire with X-EDS collected along the line (yellow) with the corresponding elemental profile for Nickel (green), Boron (blue) and Carbon (red). (b) Enlarged elemental profile of Nickel.

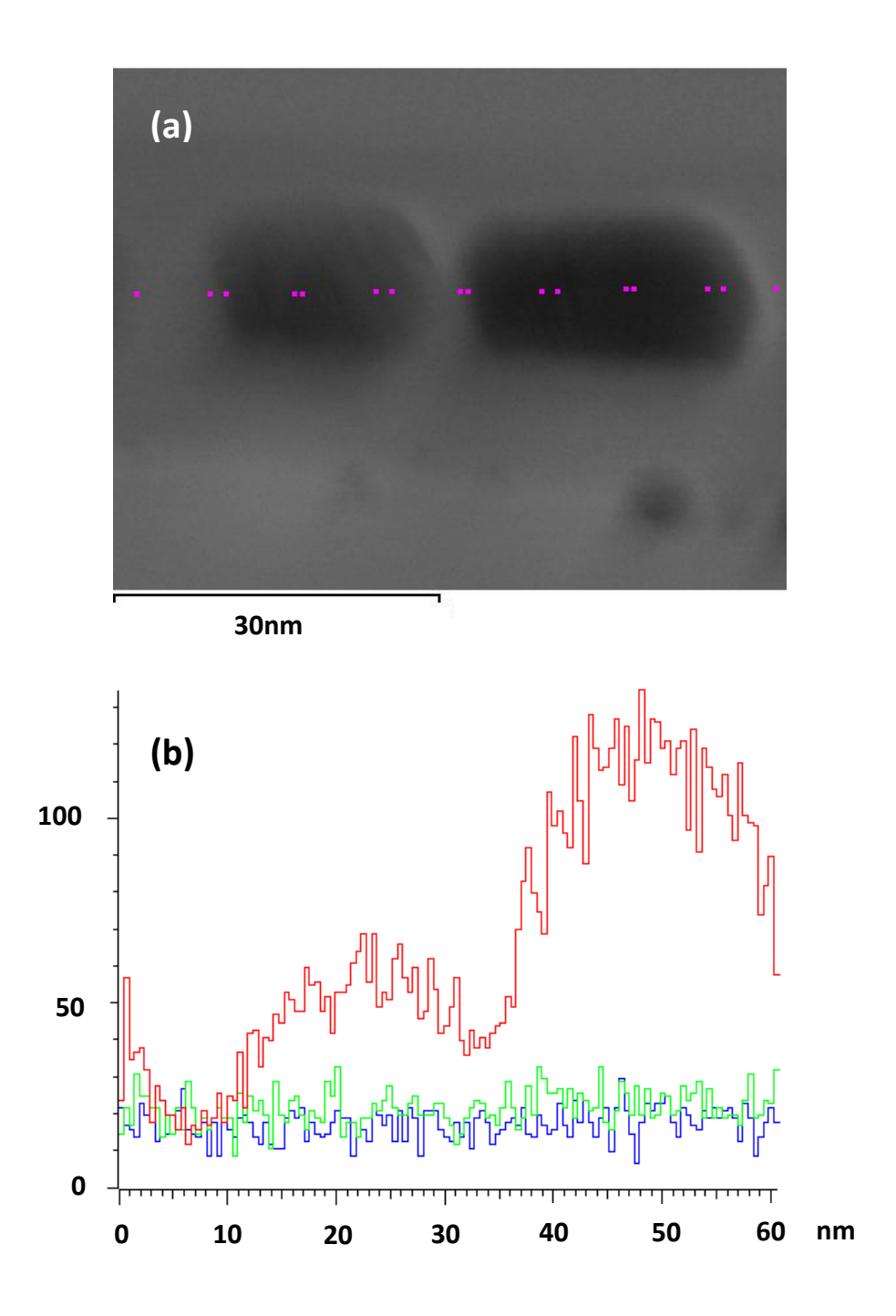


Figure 4.8 (a) Line scan across two adjacent nanoparticles. (b) Corresponding concentration profiles of Nickel (red), Boron (green) and Carbon (blue) appended to one another for comparison.

In order to obtain a better spatial profile for Boron and Carbon, a region of a suspended nanowire i.e. well isolated from the supported carbon film was chosen and a line scan was performed. The region selected had no embedded nanoparticle to avoid any interference. Figure 4.9 displays the line scan results.

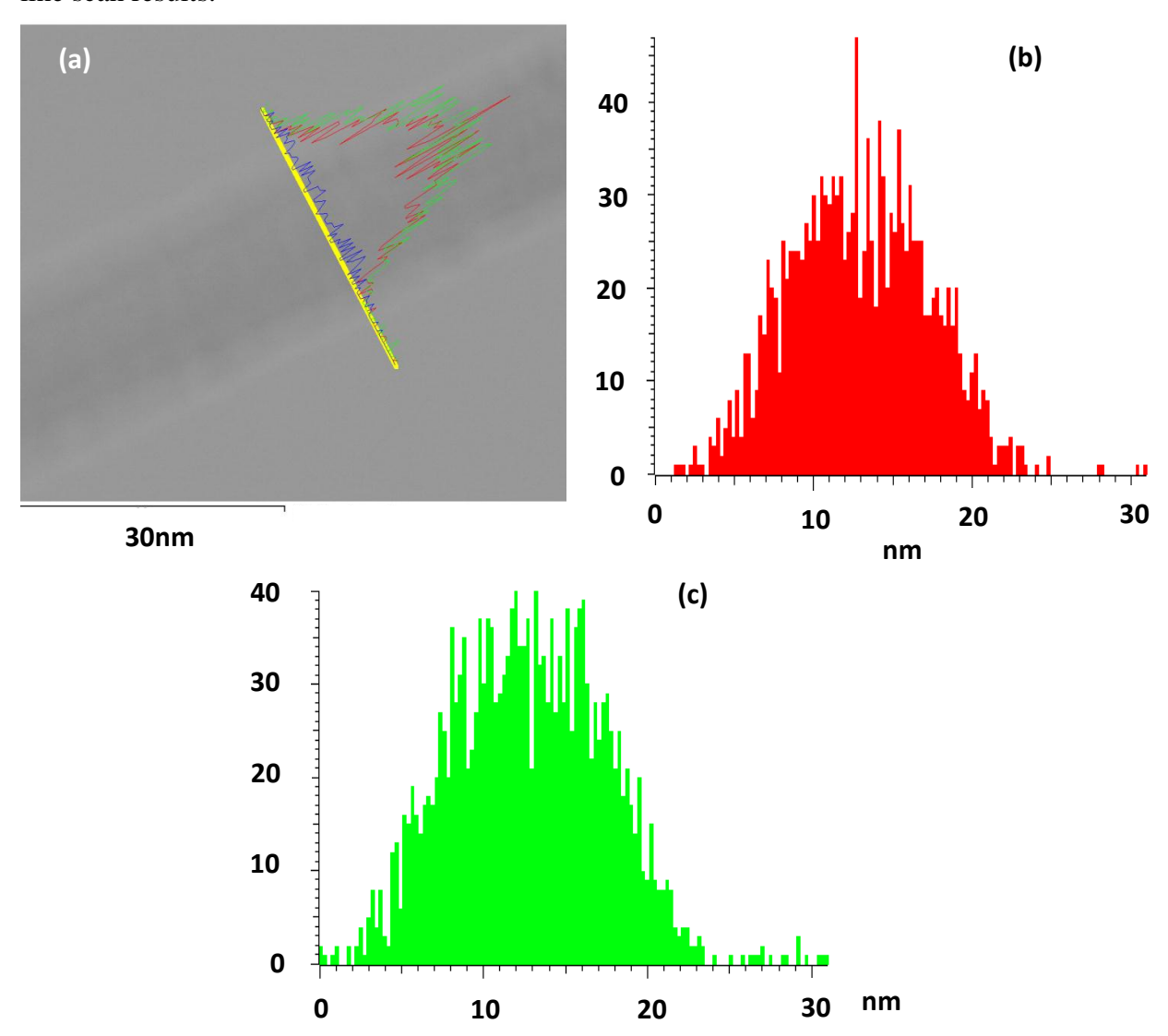


Figure 4.9 (a) Image of a section of the heterostructured nanowire with X-EDS collected along the line (yellow) with the corresponding elemental profile for Nickel (blue), Boron (red) and Carbon (green). (b) and (c) show the enlarged elemental profiles along with the X-ray counts for Boron and Carbon respectively.

Interestingly, when the separate section was analyzed a clear peak for Boron was obtained (figure 4.9c) confirming its presence in addition to Carbon and Nickel. The corresponding line scan X-EDS profiles show a distinct variation of Boron and Carbon across the nanowire. These results suggest that the nanowire could be composed of a form of Boron Carbide. However, the atomic percentages indicate a near 1:1 ratio of Boron and Carbon which is quite unlikely since the forms of Boron Carbide more widely found are $B_{13}C_2$ and B_4C [33, 34]. Figure 4.10 shows the X-EDS results from an area scan of a region of the heterostructured nanowire.

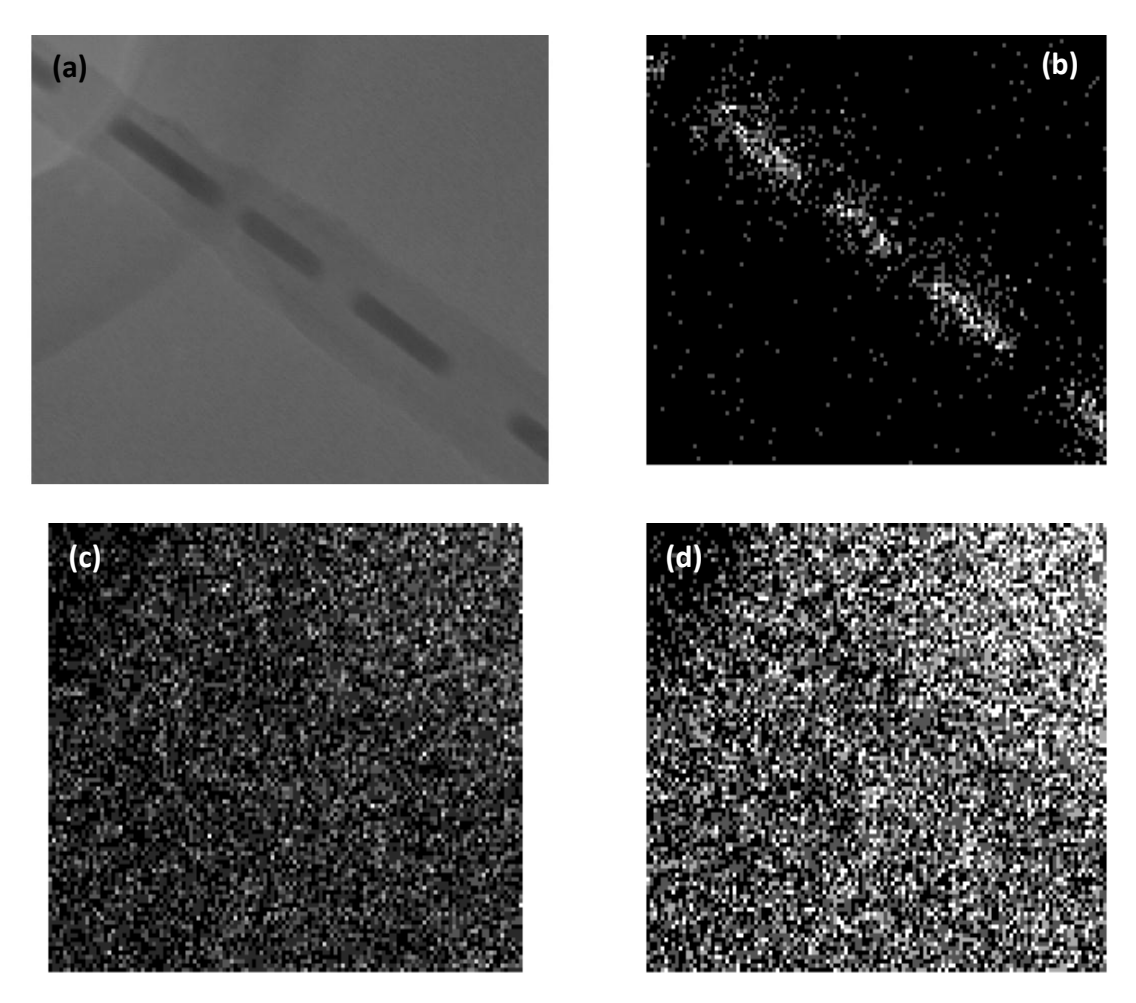


Figure 4.10 (a) Image of a section of the heterostructured nanowire with X-EDS collected from the entire area. (b), (c) and (d) show the area maps of Nickel, Boron and Carbon respectively.

The regions corresponding to Nickel are clearly mapped as shown in figure 4.10b, however, no such clear mapping is observed in case of Boron or Carbon. From the Carbon map it can be understood that the distinct profile corresponding to the nanowire region is not observed due to the rich concentration of background Carbon film. In case of Boron map, no clear evidence is observed due to the overlap of Carbon peak with Boron peak in the X-EDS. From figures 4.7, 4.8, and 4.10 it is observed that the Boron or Carbon concentration profiles don't distinctly show up in the regions of the nanowire with Nickel nanoparticles embedded.

The results clearly indicate that the STEM-XEDS technique doesn't seem to be effective in detecting Boron and Carbon in the vicinity of Nickel. This could be due to the preferential scattering of the electron beam and X-ray generation from a heavy element (Nickel) in comparison to the lighter elements (Boron and Carbon). Therefore, an advanced technique which could investigate the presence of Boron, Carbon and Nickel simultaneously is required to affirmatively confirm the presence or absence of all three elements in the vicinity of one another. For this purpose, elemental mapping using the Energy Filtered Imaging technique making use of the Electron Energy Loss Spectroscopy (EELS) was adopted. One of the important reasons for the choice of this technique is that the energy resolution of EELS is about 1eV which is much better than the energy resolution of X-ray spectrometry which is about 135eV. The following sections present a brief overview of EELS and the imaging technique.

4.2.3 Electron Energy Loss Spectroscopy (EELS)

Electron Energy Loss Spectroscopy is the analysis of the energy distribution of the electrons that have passed through the specimen. This will include the electrons that have suffered energy loss (inelastic scattering) or no loss (elastic scattering). Analyzing this energy distribution can

provide a tremendous amount of information about the chemistry and electronic structure of the atoms of interest in the specimen. From this, vital information such as bonding state, nearest neighbor atomic structure, free electron density, band gap and such can be obtained. In order to analyze the energy loss spectrum, the magnetic prism technology is adopted. EELS can detect and identify all elements of the periodic table and in particular is very effective for lighter elements. The choice of this technique for boron detection is therefore well justified. In addition, EELS offers even greater spatial resolution when compared to XEDS. The energy loss spectrum can be roughly divided into low-loss and high-loss regions with the distinction approximately provided by the 50eV point. Figure 4.11 shows a typical core energy loss spectrum for Nickel.

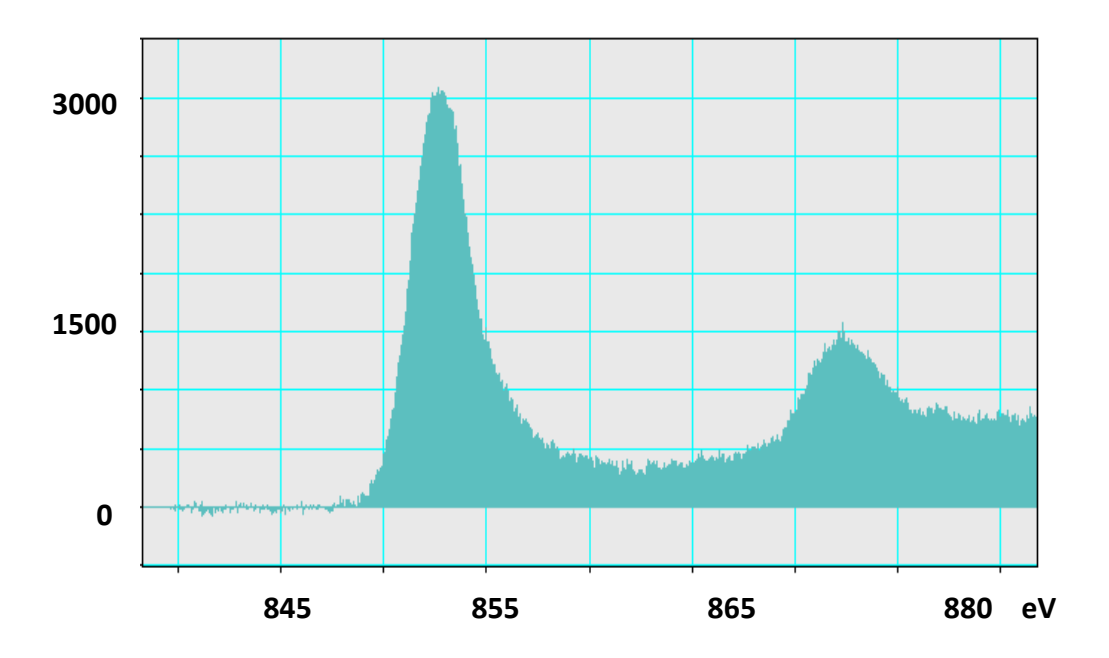
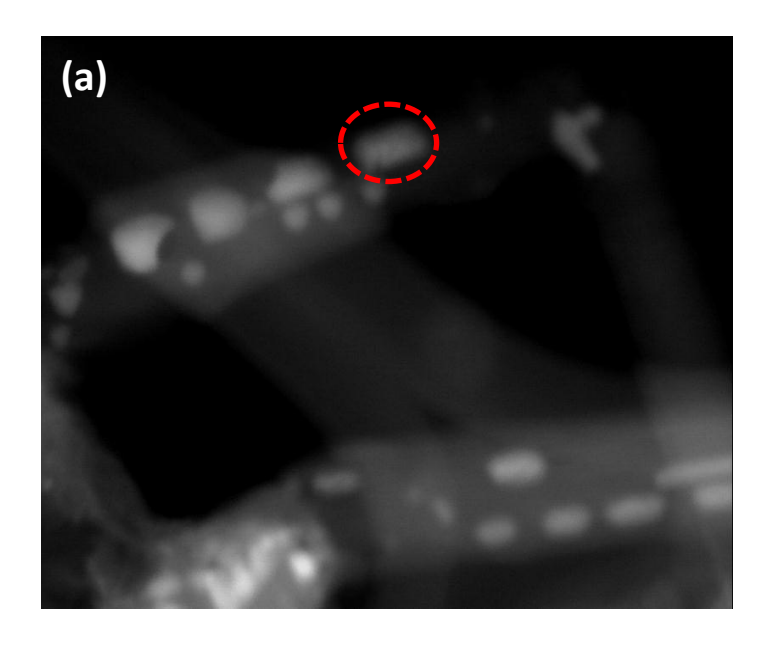


Figure 4.11 A typical core energy loss spectrum for Nickel after background subtraction.

The low loss regions contain information about the more weakly bound conduction band electrons while the high loss regions contain information about the more tightly bound core shell electron in addition to details on bonding and atomic configuration. The first zero loss or 'elastic' peak represents electrons which are transmitted without suffering any measurable energy loss

include those which are scattered elastically in the forward direction and those which have excited phonon modes for which the energy loss is less than the experimental energy resolution. Inelastic scattering from the outer shells is visible as a peak (or a series of peaks) in the 5-50eV region. Overall signal intensity drops rapidly with increasing energy loss reaching negligible levels at about 2KeV. Superimposed on this smoothly decreasing intensity are features which represent inner shell excitation. These features take the form of edges rather than peaks i.e. the inner shell intensity rising sharply and then falling more slowly with energy loss. The sharp rise occurs at the ionization threshold and the energy coordinate is the approximate binding energy of the corresponding atomic shell. Since inner shell binding energies depend on the atomic number of the scattering atom the ionization edges are characteristic of the elements present in the specimen. When viewed in greater detail both the valence electron (low loss) peaks and the ionization edges (high loss) possess a fine structure which reflects the crystallographic or energy band structure of the specimen. For spectrum acquisition the electrons with different energies are split using a magnetic prism and are collected at different positions. Having provided a brief overview of the energy loss spectrum and the acquisition method, the spectrum acquired from the Nickel embedded region of the heterostructured nanowire displaying the characteristic first ionization peak around 850eV is shown in figure 4.12.



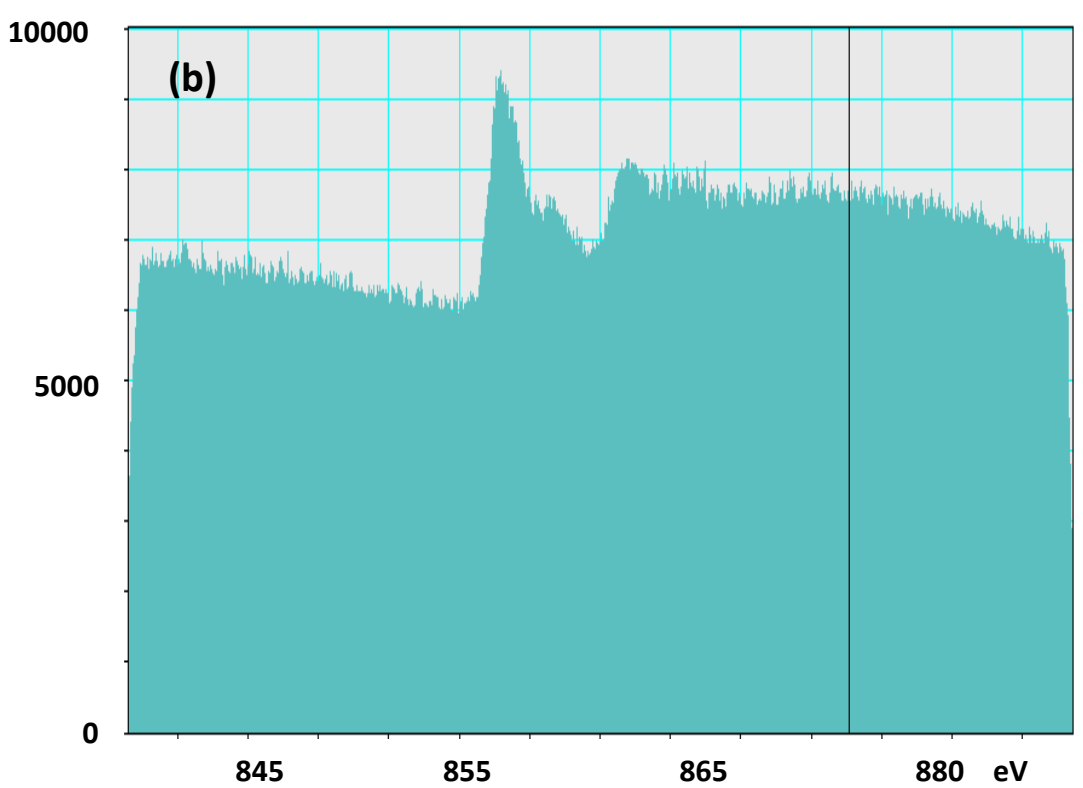


Figure 4.12 (a) Dark field STEM image of a cluster of heterostructured nanowires. (b) High loss spectrum around the ionization edge of Nickel (865eV) from the region marked red in (a).

From figure 4.12b the ionization edge around the value corresponding to Nickel clearly demonstrates the presence of Nickel. The above spectrum was just presented as an illustration, however, due to certain practical difficulties, elemental mapping using the Energy Filtered Imaging technique (commonly referred to as EFTEM) was adopted for detection for Boron and Carbon in the vicinity of Nickel.

4.2.4 Elemental Mapping Using EFTEM

The information carried by inelastically scattered electrons can be displayed in several ways one of them being the energy loss spectrum. One other way is to utilize directly the imaging capabilities of the microscope together with the 'energy filtering' capability of the spectrometer. When the filter is set to accept energy losses within a selected range the corresponding image formed is called the energy filtered image. For example, a zero loss image is formed by only allowing the elastically scattered electrons using an energy selection slit. A zero loss image has the advantage of higher contrast and therefore better resolution than an unfiltered image. When an EFTEM image is formed using the ionization edge it corresponds to the elemental map. For quantitative mapping, two images from the background preceding the edge and one after the edge is obtained. The two images preceding the edge are used to extrapolate the background under the edge and this extrapolated background when subtracted from the post edge image gives the accurate and quantitative elemental map. To form a specific filtered image the energy spectrum is shifted until the desired energy window passes through the energy selection slit. The energy shift is achieved by changing the acceleration voltage of the TEM so that electrons of different energies stay on axis and thus in focus through the spectrometer. Figure 4.13 displays the zero loss image and the elemental maps of the heterostructured nanowire.

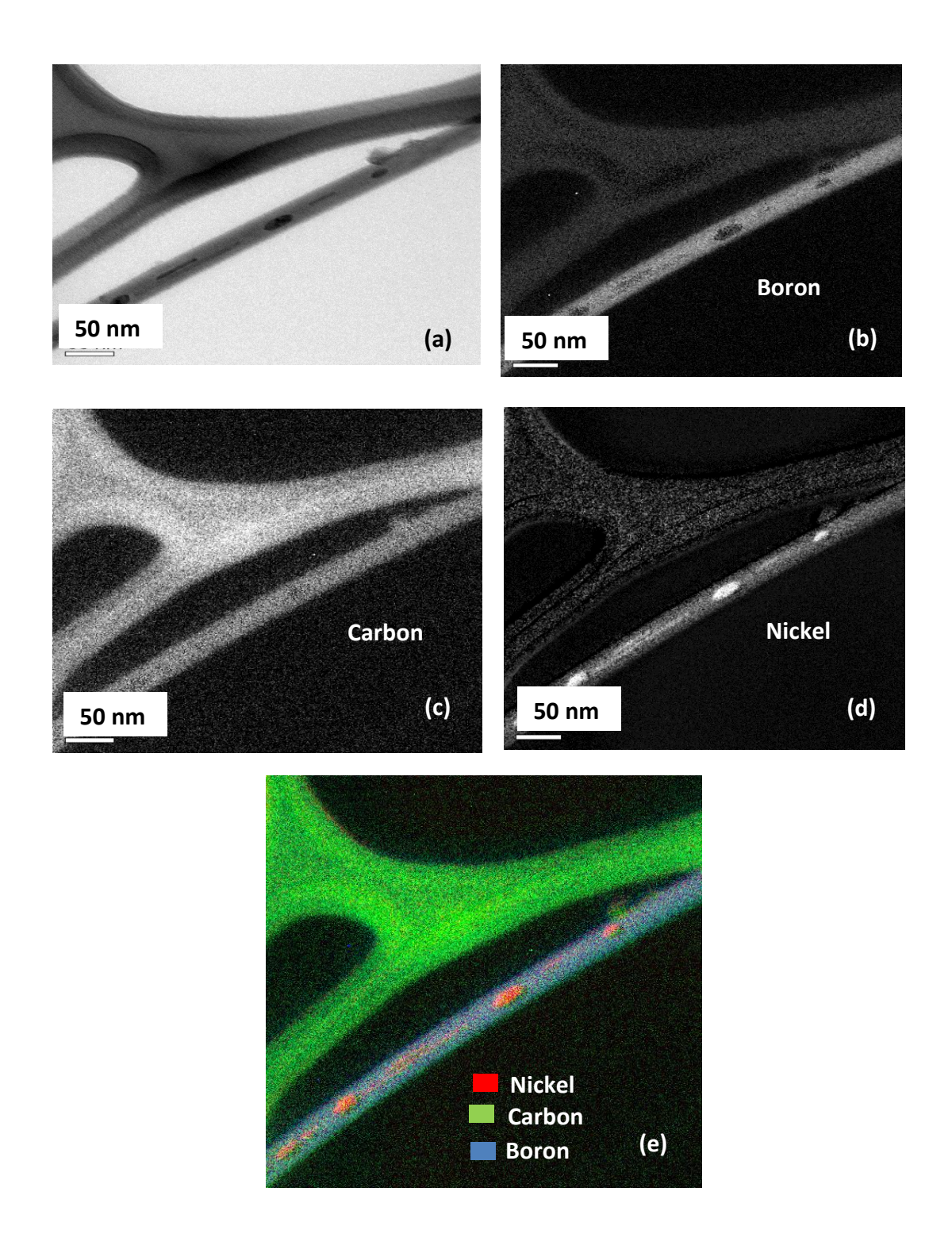


Figure 4.13 (a) Zero loss image of a heterostructured nanowire. Elemental maps of (b) Boron (c) Carbon and (d) Nickel obtained using the three window EFTEM method (e) color map of all three elements.

Some interesting results can be inferred from the elemental maps. Firstly, there is a clear evidence for the presence of Boron in the vicinity of Nickel which was not possible to be detected using the STEM-XEDS technique. This wide difference in the capabilities of the two techniques could be due to a more effective detection of lower atomic number elements using the energy loss technique than the XEDS technique. This point was mentioned before but it is instructive to reiterate here. Unlike the dominant Carbon peaks that showed up in the STEM-XEDS suggestive of an appreciable Carbon concentration in the nanowire, the map corresponding to Carbon (figure 4.13c) conveys a faint Carbon concentration in the nanowire. In addition to Boron detection, the results also indicate a rich concentration of Boron in the nanowire suggesting that the composition could be B₄C, a stable form of Boron Carbide. However, to draw conclusive results on the composition it is necessary to carefully analyze the fine structure details near the ionization edges of the elements in the energy loss spectrum. Comparing them with standard results could provide insight into the composition of Boron Carbide regions of the nanowire.

Chapter 5

Electro-Mechanical Characterization and Model Verification

This chapter presents the results of the buckling experiment for electro-mechanical characterization of the segmented nanowire. The technique and the method are first outlined followed by the discussion of the measurements. This is followed by the application of the model developed to examine the difference between the results predicted and observed. Significant deviations are observed which led to buckling experiments on bigger nanowires to understand the reasons behind the deviation.

5.1 Buckling Experiment

An individual segmented nanowire was buckled in-situ for the electro-mechanical characterization of the structure as a force sensor. First step involved picking a bundle of nanowires from a cluster as shown in figure 5.1.

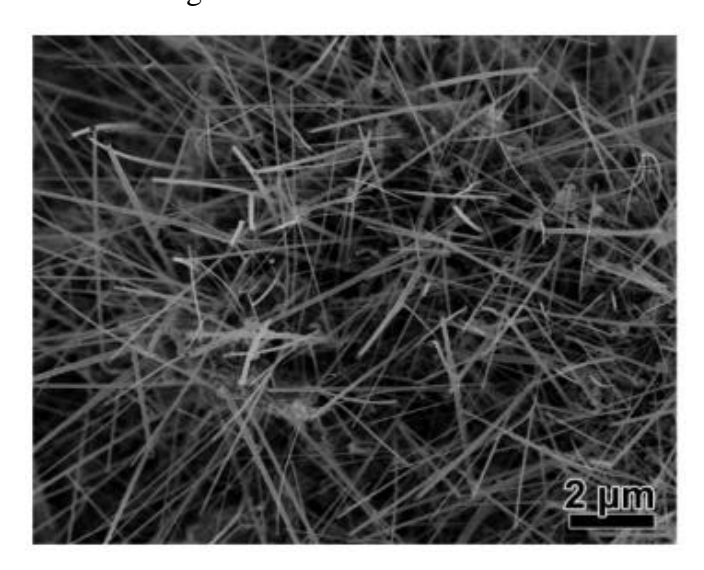


Figure 5.1 A SEM image showing a cluster of the segmented nanowires.

Buckling a single nanowire with simultaneous observation requires the experiment to be performed in a TEM with a state of the art manipulator that can be inserted into the microscope.

This purpose was served by a Scanning Tunneling Microscope (STM) probe built in a TEM (CM30) holder (Nanofactory Instruments AB, ST-1000) [35].

To fix the nanowire bundle to the probe holder, the bundle was first attached to a 0.25mm thick gold wire which then was attached to the probe holder. Gold wire is used as the interface to ensure good conductivity. The free end of the nanowire is contacted by the STM probe tip. The probe is then translated along the axis of the nanowire. The other end of the nanowire, which is hinged to the gold wire, experiences an equal and opposite force creating the required force configuration for inducing buckling. It was initially attempted to measure the force during buckling, but the method failed. Therefore, end displacement of the nanowire was chosen as the parameter for mechanical characterization. These were measured from the TEM images.

The end displacement ED (figure 5.2) is given by

$$ED = l - X \tag{5.1}$$

where X is the x-coordinate of the end of a buckled nanowire for a terminal angle α .

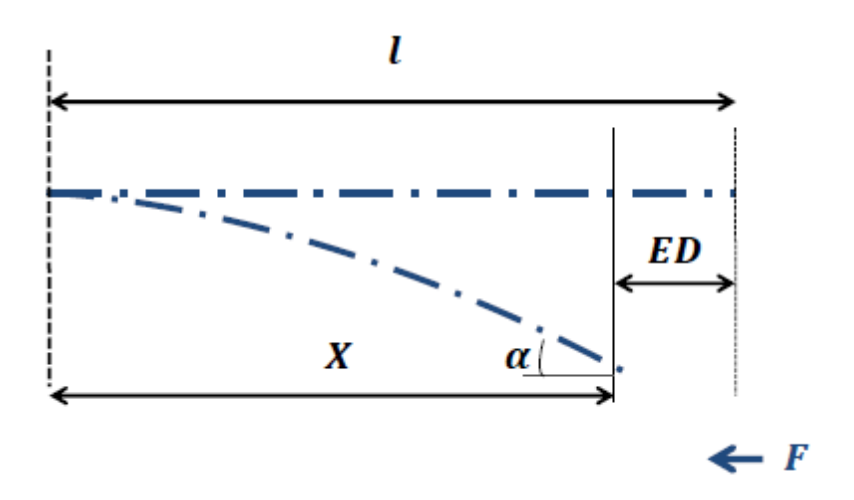


Figure 5.2 Schematic showing the end displacement.

Displacement percentage is given by

Displacement% =
$$100 ED/l = 200(1 - E(p)/K(p))$$
 (5.2)

where K(p) and E(p) are the complete elliptic integrals of the first and second kind respectively.

While performing the displacement measurements the current through the nanowire was simultaneously measured using a nanoampere meter built within the manipulator. For a constant bias of 2.5V the current is found to increase as the external force increases. However, no such increase in current is observed when a similar measurement was performed on a homogeneous Boron Carbide nanowire strongly suggesting that the rise in current could be due to the continuous decrease in the separation between the lower edges of the center pods with increasing force. TEM images during different stages of the electro-mechanical characterization are displayed in figure 5.3.

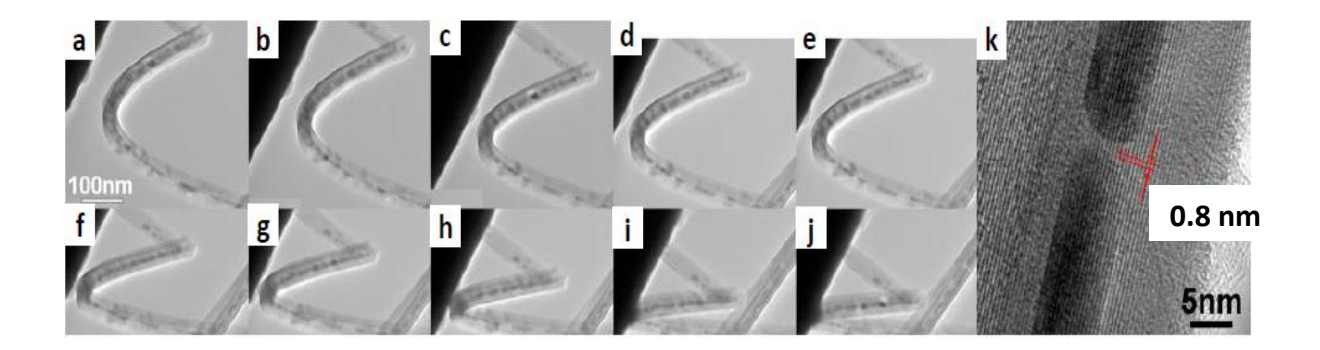


Figure 5.3 TEM images during different stages of the electro-mechanical characterization.

The currents measured are plotted against the corresponding displacement% values as shown in figure 5.4.

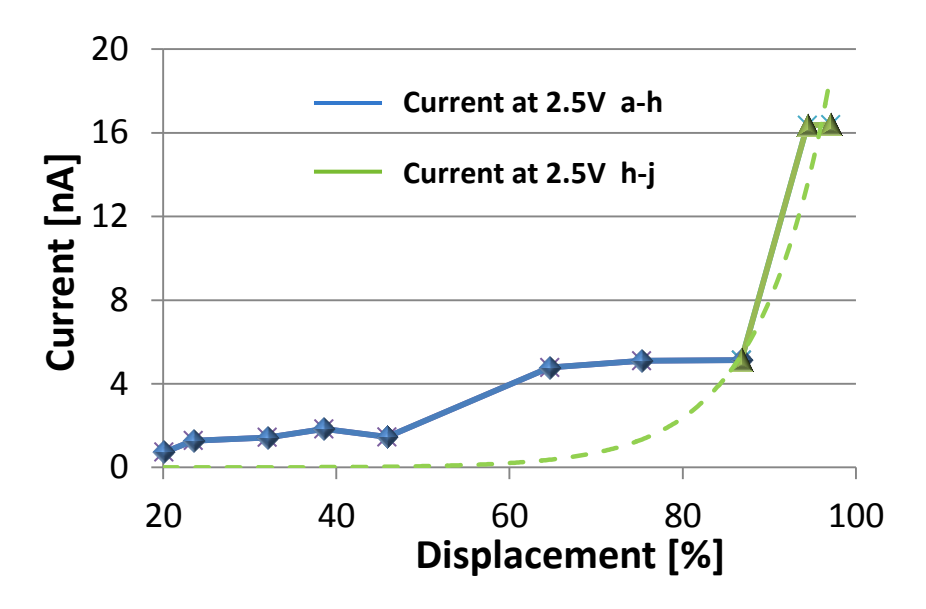


Figure 5.4 Experimental Current-Displacement% curve.

The irregularities in the first part of the plot make it difficult to intepret whether the change is non-linear. However, the interesting feature is the jump (region marked green in figure 5.4). This is indicative of a strong non-linear change. The current value increased from 5.13nA to 16.36nA as the displacement% increased from 94.4% to 97% i.e. an increase of about 200% in the current for a very small change in the end displacement.

5.2 Model Verification

In order to test the model, the nanowire is assumed to be composed of B₄C with embedded Ni particles. For this structure the barrier height was calculated to be 1.09eV based on the work function of Ni [36] and electron affinity of B₄C [37]. Young's modulus of the B₄C nanowire was taken to be 457GPa [38]. For the structural dimensions, the initial center pods separation was taken to be 0.8nm (figure 5.3), half length of the wire 400nm, outer diameter 20nm and diameter of the embedded pod 7.5nm. These dimensions were chosen based on the TEM images. The

theoretical current-displacement% curve simulated using the model with the above input parameters is shown in figure 5.5.

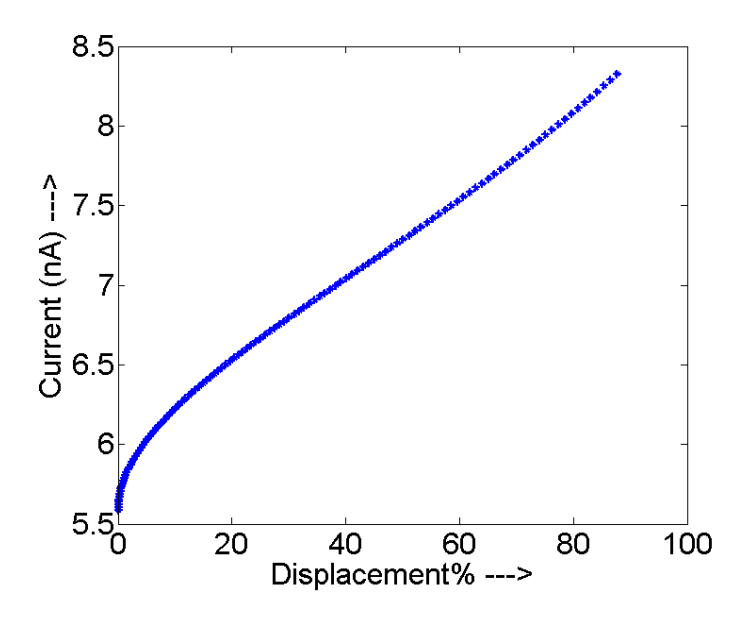
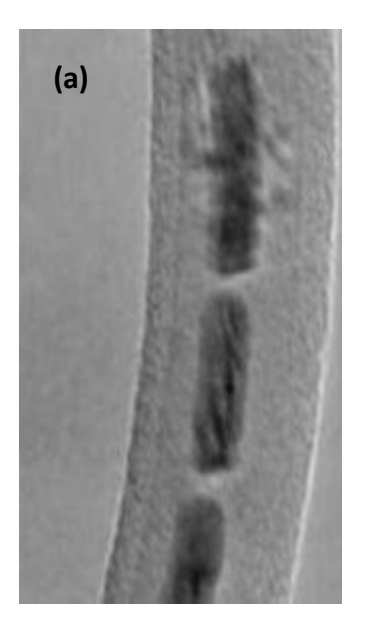


Figure 5.5 Predicted Current-Displacement% curve for Ni-B₄C-Ni segmented nanowire.

The end displacement was considered for the range from zero to about 95% (based on figure 5.4). This corresponds to deflection angles close to cross over. A clear disagreement between the model predictions and the experiment is evident, especially w.r.t. the magnitudes of the currents observed. Nevertheless, the model predicts an interesting non-linear trend. Lack of agreement between the theoretical results and the experimental values could be due to many reasons such as temperature effects – altered Fermi-Dirac distribution, inelastic scattering, noise in measurement etc. However, the striking feature in the observed trend is the jump in the current measured. To understand the reason for this significant deviation, another experiment was carried out on a slightly bigger structure. This time the experiment was confined to only mechanical deformation. Bigger structure enabled higher magnifications during buckling process and thereby a direct

observation of the separation changes. The high resolution images revealed a surprising trend as shown in figure 5.6.



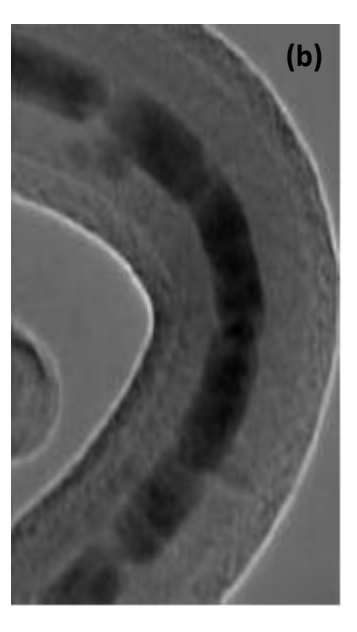


Figure 5.6 (a) Segmented nanostructure for small end displacement (b) same structure for large end displacement.

Contrary to the expected rotation of the center pods induced by buckling, the images reveal that the center pods are actually moving closer to each other along the axis for large end displacement. A near 100% reduction in their initial separation is observed strongly suggesting that axial compression is taking place. Moreover, the curvature of the nanowire for large deformation doesn't correspond to the smoothness in the curve for the case of pure buckling i.e. during pure buckling even when the ends cross over, the axis has a smooth curve at the center. These observations strongly suggest that the process occurring in the experiment violates the condition of pure buckling. Hence, the simple mechanical model developed is inapplicable to make predictions for the force-separation change. Detailed simulations are required to simulate the observed behavior. The drastic jump can be easily understood as the consequence of the center pods axially coming closer and squeezing into one another which causes a drastic

reduction in the barrier width and hence the observed enhancement. Greater reduction in the axial separation between the pods makes the predicted rotation effects on tunneling insignificant. Taking the cue from this experimentally observed behavior, an interesting question was raised – will a similar enhancement be observed if the electron transport was ballistic i.e. if the wave nature of electron was preserved across the entire structure? Some interesting results were obtained using quantum transport formalism and are discussed in the next chapter.

Chapter 6

Quantum Transport - An Effective Non-Hermitian Hamiltonian Approach

The segmented nanostructure is a quantum system characterized by discrete energy levels. When there is no interaction with the external world (continuum) the system is 'closed' and the discrete levels correspond to bound states. However, when the system is coupled to the continuum (leads) it becomes 'open' and the states become quasi-bound due to their continuous decay to the outside world. The interaction is through 'channels' which open for energies beyond a certain threshold value. The decay causes the levels to acquire a 'complex' width and the states are no longer the eigenstates of a Hermitian Hamiltonian but are the eigenstates of an effective non-Hermitian Hamiltonian. The Hamiltonian for the quantum system along with the continuum would be Hermitian, but due to the infinitely many states in the continuum a meaningful basis size for representing the Hamiltonian cannot be possible. The study of the open quantum system while still considering the effects of the continuum is done through the effective non-Hermitian Hamiltonian theory [39]. The Hilbert space of the open system is divided into two mutually orthogonal subspaces with the help of orthogonal projectors P and Q which satisfy the following relations,

$$P + Q = 1,$$

 $PP = P, QQ = Q, PQ = QP = 0$ (6.1)

Then the solution of the stationary Schrodinger equation

$$H\Psi\rangle = E\Psi\rangle \tag{6.2}$$

has two parts

$$\Psi \rangle = P\Psi \rangle + Q\Psi \rangle \tag{6.3}$$

If one class of states is eliminated (for ex. Q class), the equation for the wave equation of the complementary class is obtained (P class) as

$$H_{eff}P\Psi\rangle = EP\Psi\rangle \tag{6.4}$$

where
$$H_{eff}(E) = PHP + PHQ(1/(E - QHQ))QHP$$
 (6.5)

The continuum states are grouped within class Q while those of the discrete quantum system belong to class P (figure 6.1). The second term refers to the multiple excursions to the continuum with return to the quantum system.

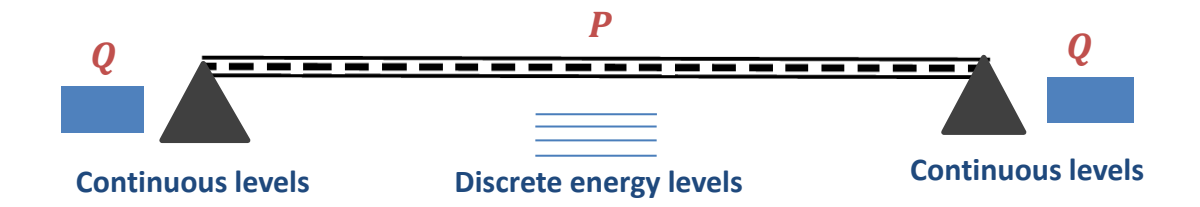


Figure 6.1 Segmented nanostructure with discrete energy levels is assigned to subspace P while the leads with continuum levels are assigned to subspace Q.

 H_{eff} is the effective Hamiltonian for the quantum system which is energy dependent and fully takes into account the coupling to the continuum without the issues of infinite basis. It is non-Hermitian because it has an anti-Hermitian part which is a result of the opening. The matrix elements of the effective Hamiltonian take the form [10, 39]

$$H_{eff}(E) = PHP + U(E) - (i/2)W(E)$$
 (6.6)

PHP corresponds to the matrix elements of the quantum system in the absence of coupling. U corresponds to the shift in the energy levels while W represents the complex widths the states acquire. Form of U and W can be found in [10]. Assuming the matrix elements of U and W are smooth functions of energ, their energy dependence can be neglected if the region of interest is concentrated in a small energy interval. With the help of effective Hamiltonian, transmission from channel a to b (from the left to the right lead) is given by

$$T_{ab}(E) = |Z_{ab}(E)|^2$$
 (6.7)

where $Z_{ab}(E)$ is the transmission amplitude given by the expression in [10].

Resonances are a result of the poles of the transmission amplitude which happen to be the complex eigenvalues of the effective Hamiltonian which take the form

$$\varepsilon_r = E_r - (i/2)\Gamma_r \tag{6.8}$$

As the coupling to the continuum is increased, rearrangement of the widths occur leading to a phenomenon referred to as 'superradiance'. It has been shown that the maximum transmission occurs during this transition. The current through the structure depends on the transmission and since for sensing applications, the current has to be maximized the following study begins with the condition of superradiance transition. Before deformation, the potential profile is as shown in figure 6.2.

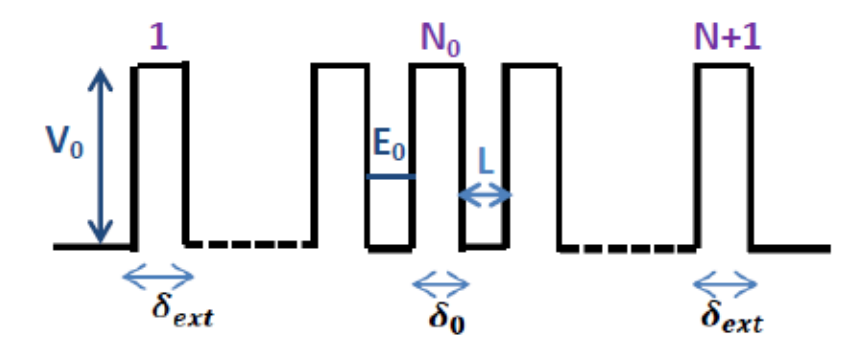


Figure 6.2 Potential profile of the structure before deformation. All barriers have equal width. The ends correspond to the barrier between the leads (continuum states) and the end pod structures.

Figure 6.2 shows N+1 barriers which implies N wells (pods) with the center barrier indexed as N_0 . The barrier height is denoted as V_0 and the energy level of interest within each well of length L is represented by E_0 . For long structures the superradiance transition has been identified to occur when the ratio between the external barrier width δ_{ext} and the internal barriers' width δ_0 (before deformation all the barriers have the same width) is ½ [10]. In order to be able to determine the transmission from equations 6.8 and 6.9, the effective Hamiltonian for the structure has to be obtained. This is given by the open 1-D tight binding model with matrix elements of the effective Hamiltonian in the site representation as shown

$$H_{eff nm} = E_0 \delta_{nm} + \Omega \left(\delta_{n+1,m} + \delta_{n-1,m} \right) + (u - (i/2)\gamma) \left(\delta_{n,1} \delta_{m,1} + \delta_{n,N} \delta_{m,N} \right)$$
(6.9)

where Ω is the coupling between the wells.

The effect of opening is incorporated through energy shift u and level broadening γ for the energy levels in the left and the right extreme 'pods' (wells) which are coupled to the left and the right continuum states (leads). The explicit expressions for Ω , γ and u can be found in [10]. Due

to the coupling Ω each discrete level in each well splits into a band of N levels. Therefore, if transmission is considered only for the mini-band centered around E_0 the number of resonances that would be observed are N (equation 6.9). However, as the coupling to the external is increased the resonance peaks broaden and at superradiance transition since restructuring of the complex widths occur, some of them overlap i.e. the levels coincide acquiring a broad width and are referred to as the superradiant states. The number of superradiant states depend on the number of open channels. For a system with N discrete states coupled to the continuum through M channels, the number of superradiant states equals M and beyond the superradiant transition (as the coupling is increased) the superradiant states decay into the continuum leaving the remaining N-M states trapped within the quantum system whose widths continue to decrease beyond transition. For N=5, L=2nm, δ_0 =0.2nm and δ_{ext} =0.1nm, $E_0 \sim 2$ (in units of 0.0318eV which corresponds to Planck's constant and electron mass equal to 1), the resonance structure is as shown in figure 6.3. Since there are two channels, one each coupling the left and the right continuum with the quantum system, at superradiance transition two of the five quasi-bound states merge to form superradiant states which is evident from the figure 6.3.

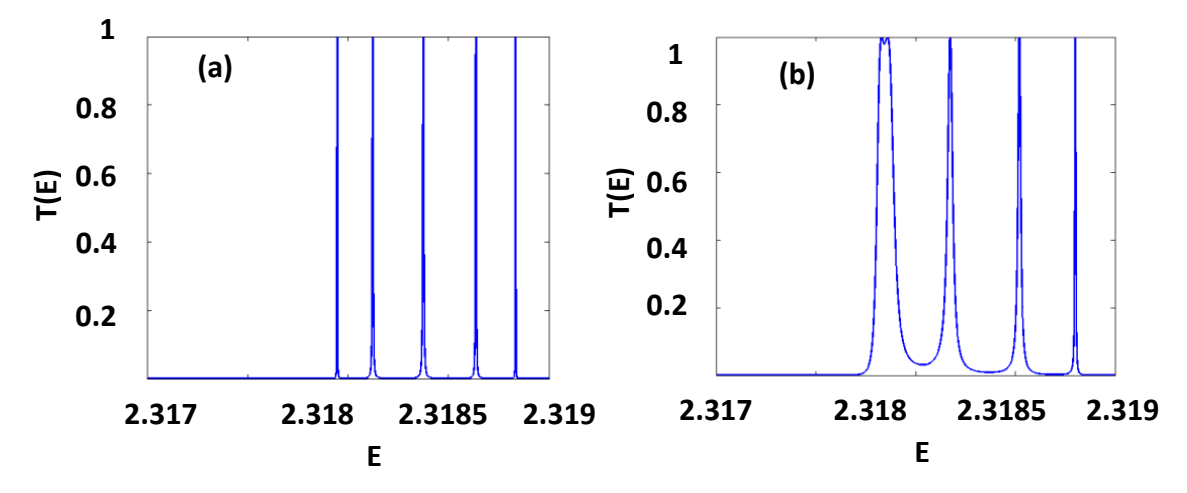


Figure 6.3 Resonance structure for (a) small coupling (b) superradiance.

Having identified the condition that transmission through the structure would be maximum at superradiance transition because of the formation of superradiant states, the question is how does an external axial force that causes a deformation as discussed in section 5.2, affect the transmission? In the quantum realm, would the reduction in axial separation between the center pods cause an enhancement similar to the observed trend? The answer is NO. When the structure is disturbed from its superradiant state by reducing the axial separation between the center pods from 0.2nm, the integrated transmission was found to decrease. Integrated transmission is given by the area under the curve corresponding to the resonance structure for energy values spanning the entire mini-band. The current through a nanoscale structure is given by the Landauer-Buttiker formula which in the limit of low temperature becomes proportional to the integrated transmission. Therefore, it is sufficient to understand the effects of force on integrated transmission which can be directly related to the current. The next question is, will increasing the number of pods, influence this reduction? For this purpose, the integrated transmission values for N=13 and 501 were obtained. In addition to showing a decrease, the most interesting observation was that the magnitude of reduction was almost identical i.e. the behavior seems to be independent of N. Before trying to understand this, it must be noted that for an ordered structure the integrated transmission becomes independent of N beyond a certain value of N [10]. But why is the decrease in the integrated transmission identical for large N on introducing a site specific disorder? What would happen if the center pods are moved away from each other (say by a stretching force)? The integrated transmission was expected to decrease (because of decreased coupling between the center wells) but the surprising result was that the reduction was identical for large N and similar in magnitude to the case of decrease in the separation between the pods

i.e. a symmetry is observed for increase and decrease of the separation w.r.t. the value corresponding to superradiant transition. Figure 6.4 shows this trend.

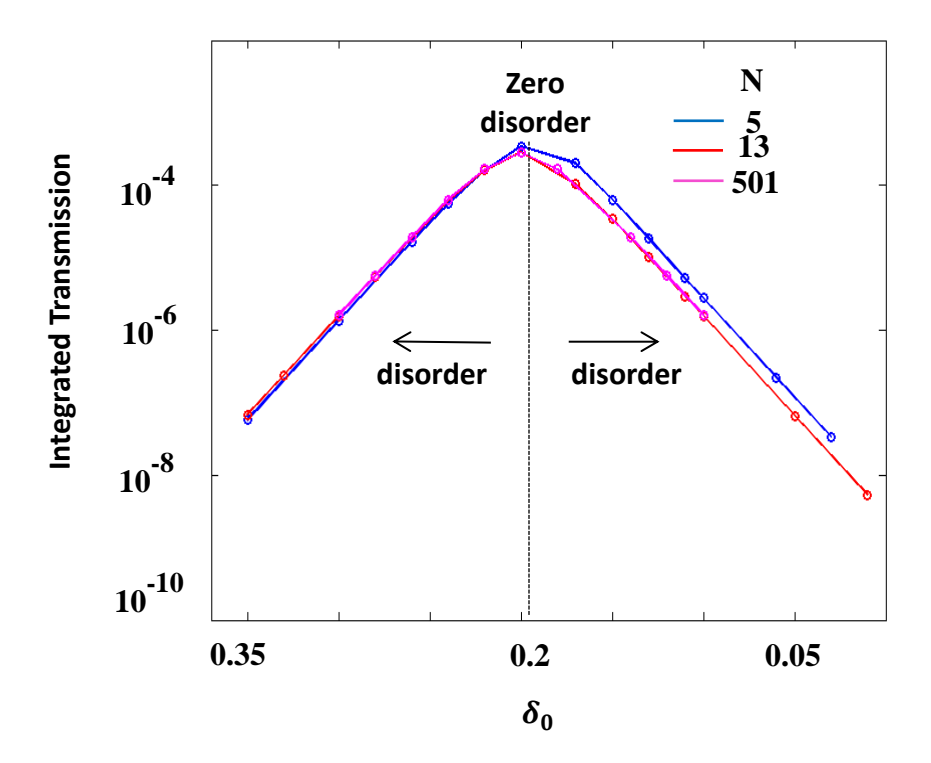


Figure 6.4 Integrated transmission vs. the separation between the center pods.

Following this interesting observation the trajectories of the eigenenergies were studied for possible explanation of the behavior. Figure 6.5 shows the trajectories of the eigenenergies on the complex plane for N=5, 13, 101 and 501 with the imaginary parts inverted in sign. All of them show a similar trend.

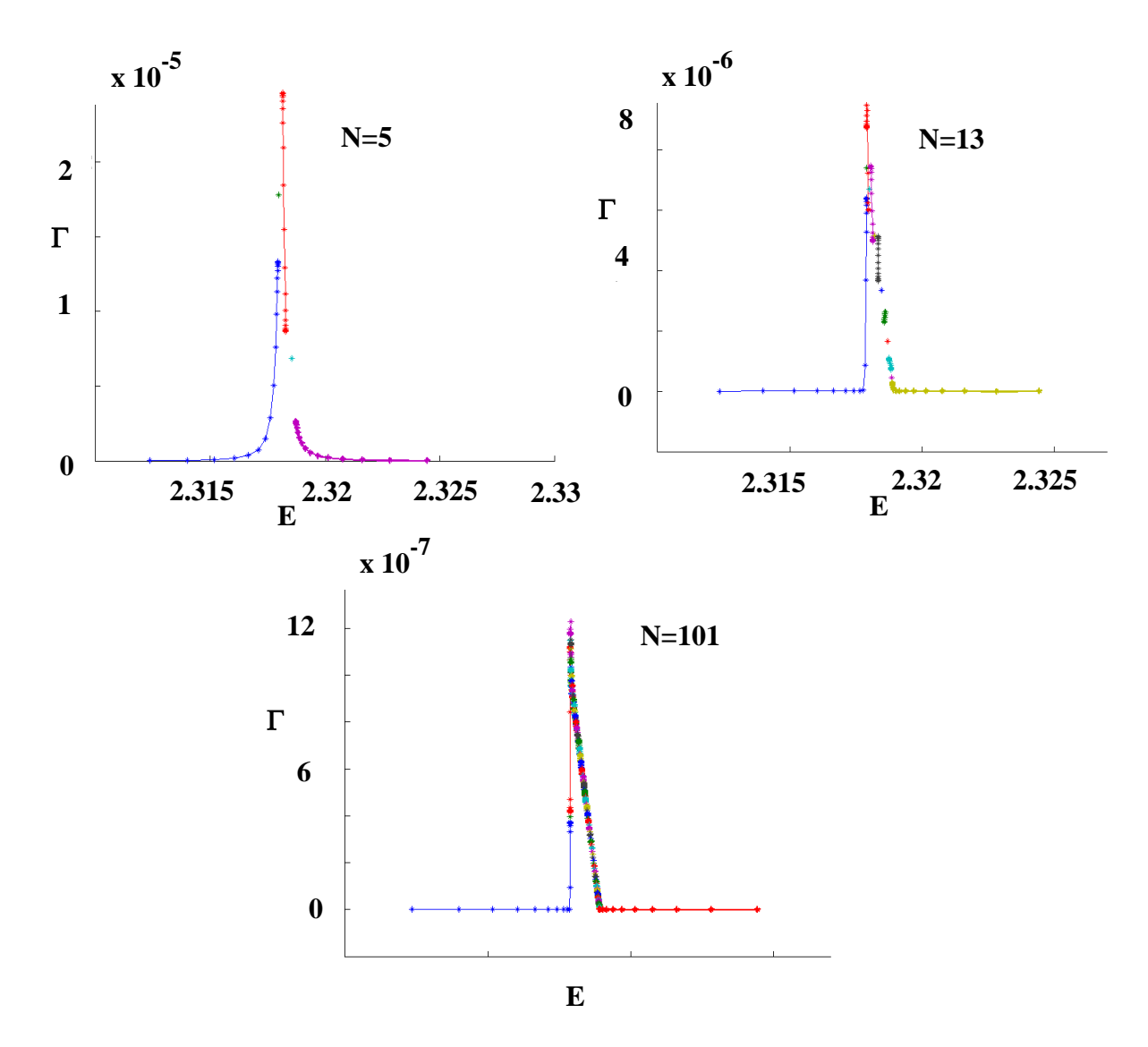


Figure 6.5 Eigenenergy trajectories in the complex plane for N=5, 13 and 101 as the center pods separation is changed from 0.3nm to 0.1nm.

The trajectories indicate that the change in separation is causing a drastic change in the values for two of the eigenenergies which were identified to be the first and N^{th} eigenenergies. This magnitude of shift in the eigenenergies suggested that the wavefunctions i.e. the eigenstates of the system could be severely affected as a result of the deformation induced disorder. Following this, the eigenstates of the system were studied for the case of N=1001.

The eigenstates of the system for N=1001 for different conditions are shown in figure 6.6.

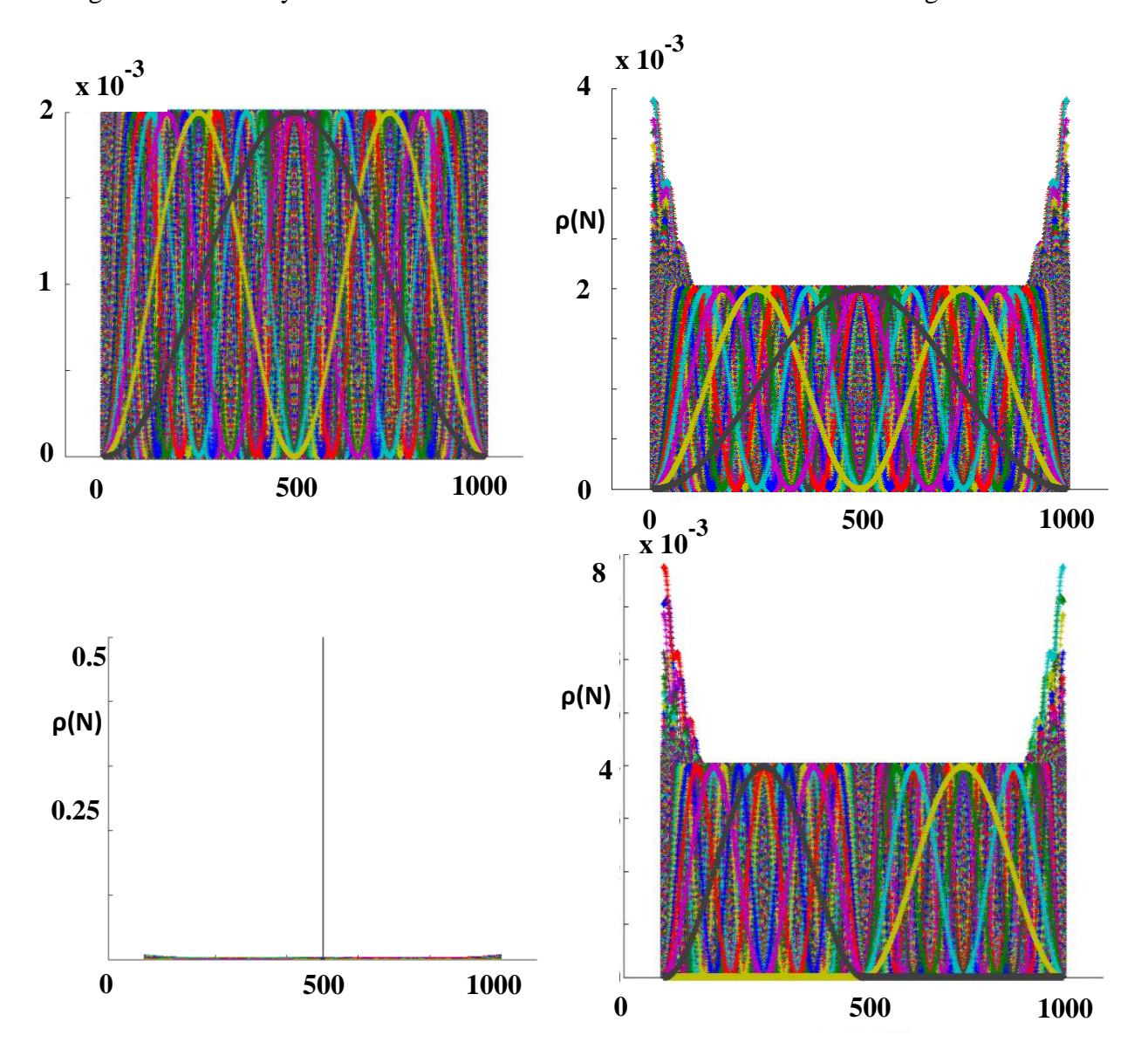


Figure 6.6 (a) Eigenstates for a closed system (b) Eigenstates for the system coupled to the continuum at superradiance transition – superradiant states are formed at the edges (c) Eigenstates for the open system with center pods separation decreased from superradiance value – a highly localized state is visible (d) Eigenstates for the open system with center pods separation increased from superradiance value – eigenstates decoupled from the left and the right half of the system.

Studying the eigenstates revealed that for the case of increase in center pods separation from the superradiant value, a signal transmitted through the system gets reflected back from the center since the eigenstate carrying the signal decays beyond that point and in case of decrease in center pods separation from the superradiant value, a signal transmitted through the system gets trapped in the highly localized state failing to reach the other channel. Thus, the decrease in the integrated transmission when the center pod separation is decreased and increased from the superradiant value can be qualitatively understood. More detailed analysis is required to uncover the reason for the symmetric drop in values w.r.t. the center pods separation. However, the nature of symmetry observed in the average transmission curve w.r.t. the coupling with the continuum which is governed by the value of the δ_{ext} [10] suggested an interesting possibility that the force induced site-specific disorder could have similarities to Anderson localization – a condition which arises as a result of random disorder introduced into the system. Furthermore, studying a particular superradiant state after increasing the center pod separation revealed a close similarity to the evolution of a superradiant state under Anderson localization [40]. This similarity is shown in figure 6.7.

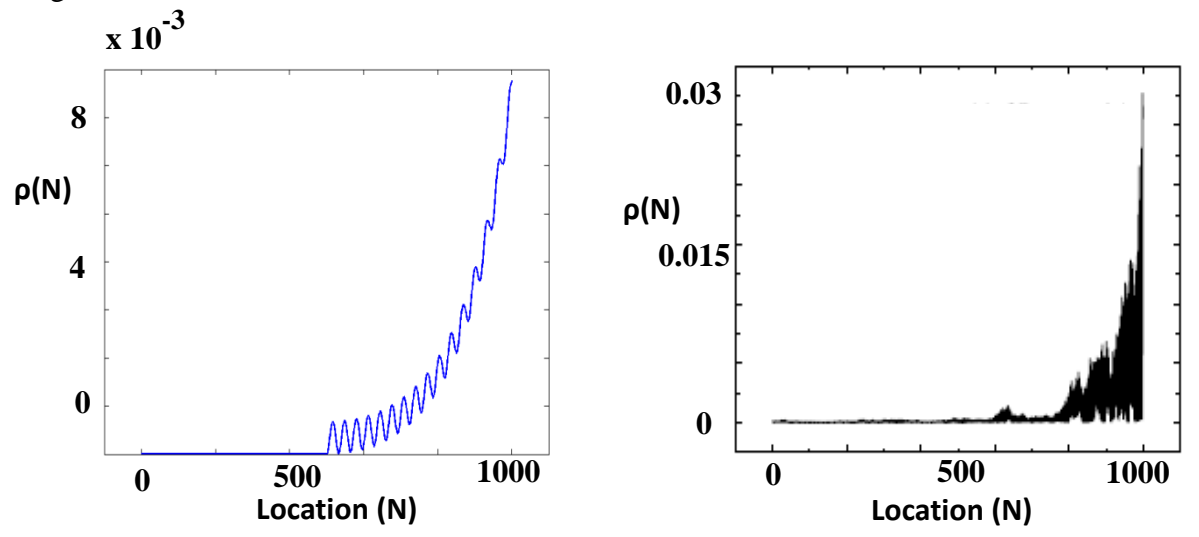


Figure 6.7 Superradiant state for (a) increased pod separation (b) Anderson Localization [40].

Random disorders leading to Anderson localization are known to exhibit repulsion between the energy levels [41]. A similar behavior is observed for the case of decrease in center pod separation when the resonance structure is studied. The case for N=5 is shown in figure 6.8.

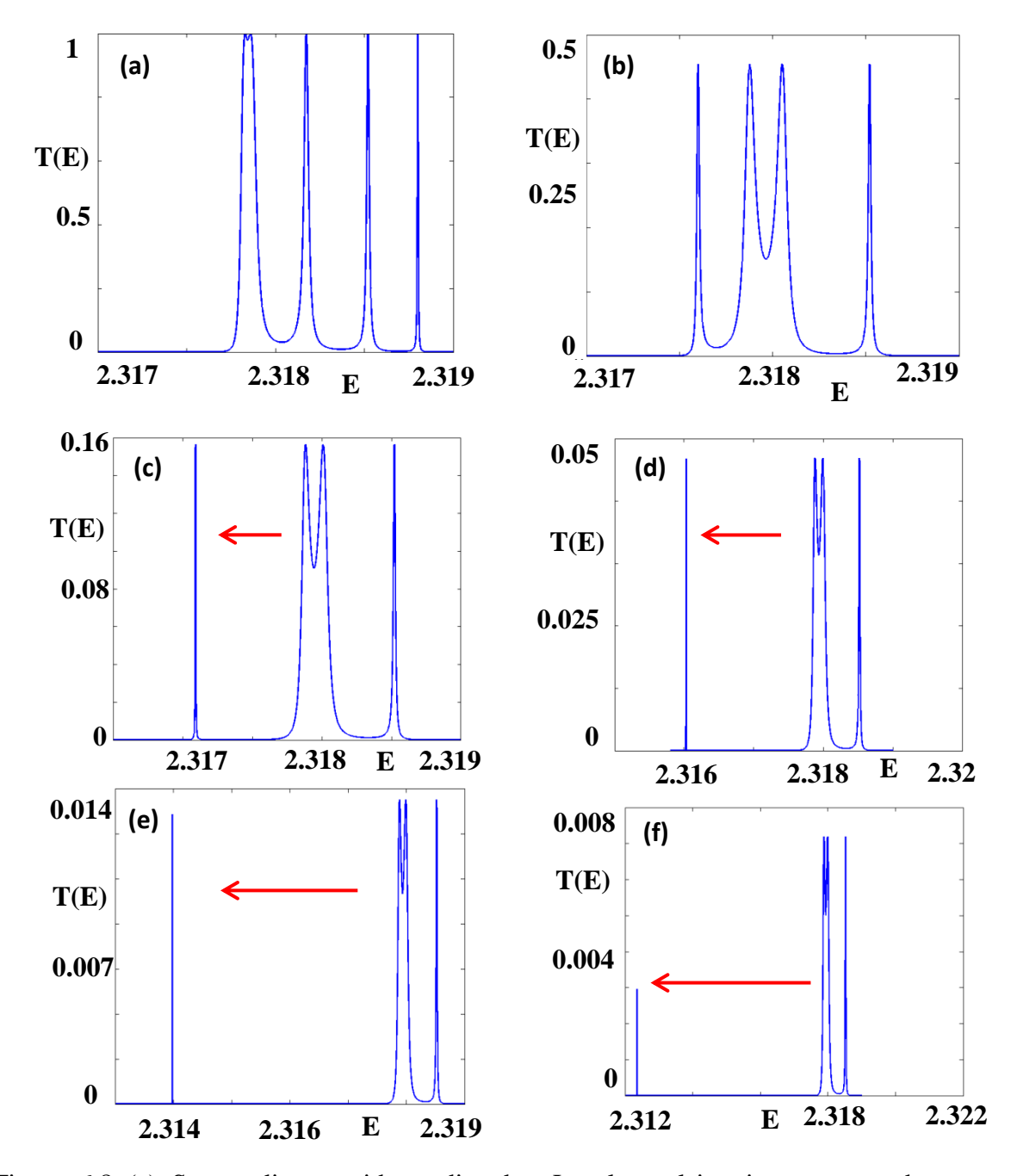


Figure 6.8 (a) Superradiance without disorder. Level repulsion increases as the center pod separation is decreased to (b) 0.17nm (c) 0.15nm (d) 0.13nm (e) 0.11nm (f) 0.1nm.

These observations suggest that the force induced disorder could be regarded as an 'embryo' of Anderson localization – a possibility that hasn't been explored before. To quantify the embryonic nature, studying the level width distribution in terms of the Wigner-Distribution distribution or the Poisson distribution of the normalized level spacing [41] or the resonance widths distribution [42] would be required. This study would be crucial because if a similarity is established the effects of random disorder could be replaced by a single 'controlled' disorder (controlled by the external force) which could have significant implications in electro-mechanical quantum information processing systems.

Chapter 7

Conclusions and Future Work

A segmented nanostructure referred to as the 'peapod' structure was studied experimentally and theoretically for a possible application as a force sensor. The theoretical model involved buckling analysis of the structure to obtain the relation between the applied force and the decrease in separation between the lower edges of the center pods. An accurate equation for the curvature of the axis of the deformed nanowire incorporating surface effects was obtained. This equation makes a provision for analyzing the deformation and the associated separation change even for large deflection angles – a result that hasn't been reported elsewhere. When surface effects are ignored the equations reduce to special mathematical functions requiring the analysis to be only numerical. However, physical information of the system in the limiting case of small deflections enables certain approximations which lead to a closed form expression between the applied force and the change in separation. This is a result specific to the problem that has not been dealt with elsewhere The closed form expression provides physical understanding of the influence of geometrical and mechanical parameters on the force-separation relation. Surface effects were also incorporated into this expression to make a provision for understanding their effects on the relation for small deflection angles. Following this a tunneling current model based on the MIM model was coupled with the mechanical model to obtain the force-current response. Some illustrative force-separation and force-current relations were simulated and certain conclusions were drawn regarding the force sensing capability of the structure. To make predictions on the force-current response for the structure in hand its electrical and parameters had to be obtained. This required estimating the composition of the segmented structure which was obtained through X-ray Energy Dispersive Spectroscopy (X-EDS) and Electron Energy Loss Spectroscopy

(EELS) studies within a Transmission Electron Microscope (TEM). The material was approximately estimated to be composed of Nickel nanoparticles embedded within a Boron-Carbide nanowire. Using the mechanical and electrical parameters of this structure, a prediction was made for the force-displacement response. Since it wasn't possible to measure the force during buckling, end displacement (measure from TEM images) was used as the input. Deviations of the predictions from that observed were studied and possible reasons discussed. The cause for the most significant deviation was identified through another buckling experiment carried out on a bigger segmented structure. It was found that instead of the rotation of the pods expected for pure buckling, the center pods were squeezed towards each for large displacements. In addition, the nature of the axis curvature observed for large displacements strongly suggested that the deformation occurring was no longer pure buckling as expected. Hence, the inapplicability of the model for this specific structure and experiment was established. Taking the cue from this kind of deformation, a series of analysis were made to understand transmission through a similar structure when deformed in the quantum realm i.e. where the wave nature of the electrons are preserved due to insufficient phase breaking scattering which is possible in case of nanoscale structures. This is also referred to as the ballistic transport. Effective non-Hermitian Hamiltonian theory was used to study the transmission. Surprising results were obtained when the structure was perturbed from its 'superradiant' configuration to the disordered state induced by the force. It was found that as the center pods separation decreases the transmission also decreases due to energy level repulsion a behavior characteristic of quantum chaos. Eigenstates and eigenenergies of the system were studied to identify the reason for this non-trivial behavior. It was found that highly localized states were formed which could trap the signal resulting in

decreased transmission. Some interesting comparisons were made to the well-known Anderson localization caused which is caused by random disorder.

To obtain a current-displacement response similar to the one observed, a more detailed mechanical analysis is required taking into account the non-ideal conditions. A more affirmative conclusion on the composition of the structure is required which could be arrived at using better material detection techniques. Finally, a possible way to quantify a probable similarity between the disorder of interest and the random disorder corresponding to Anderson localization in the quantum realm was suggested.

REFERENCES

REFERENCES

- [1] D. Rugar, R. Budakian, H. J. Mamin and B. W. Chui, *Single spin detection by magnetic resonance force microscopy*, Nature **430**, 329 (2004).
- [2] J. L. Arlett, J. R. Maloney, B. Gudlewski, M. Muluneh and M. L. Roukes, *Self-sensing micro- and nanocantilevers with attonewton-scale force resolution*, Nano Lett. **6**, 1000 (2006).
- [3] K. C. Schwab and M. L. Roukes, *Putting mechanics into quantum mechanics*, Phys. Today **58**, 36 (2005).
- [4] J. A. Sidles, J. L. Garbini, K. J. Bruland, D. Rugar, O. Zuger, S. Hoen and C. S. Yannoni, *Magnetic Resonance Force Microscopy*, Rev. Mod. Phys. **67**, 249 (1995).
- [5] S. J. Koch, G. E. Thayer, A. D. Corwin and M. P. de Boer, *Micromachined piconewton force sensor for biophysics investigations*, Applied physics letters **89**, 173901 (2006).
- [6] K. Shou, L. Dong and B. J. Nelson, *NEMS-on-a-tip: Force sensors based on electromechanical coupling of individual multi-walled carbon nanotubes*, paper presented at the IEEE/RSJ International Conference on Intelligent Robots and Systems (2008).
- [7] S. Siechen, S. Y. Yang, A. Chiba and T. Saif, *Mechanical tension contributes to clustering of neurotransmitter vesicles at presynaptic terminals*, Proc. Natl. Acad. Sci. U. S. A. **106**, 12611 (2009).
- [8] X. D. Wang, J. Zhou, J. H. Song, J. Liu, N. S. Xu and Z. L. Wang, *Piezoelectric field effect transistor and nanoforce sensor based on a single ZnO nanowire*, Nano Lett. **6**, 2768 (2006).
- [9] Y. S. Zhou, R. Hinchet, Y. Yang, G. Ardila, R. Songmuang, F. Zhang, Y. Zhang, W. H. Han, K. Pradel, L. Montes, M. Mouis and Z. L. Wang, *Nano-Newton Transverse Force Sensor Using a Vertical GaN Nanowire based on the Piezotronic Effect*, Adv. Mater. **25**, 883 (2013).

- [10] G. L. Celardo and L. Kaplan, Superradiance transition in one-dimensional nanostructures: An effective non-Hermitian Hamiltonian formalism, Phys. Rev. B 79, 155108 (2009).
- [11] G. F. Wang and X. Q. Feng, *Timoshenko beam model for buckling and vibration of nanowires with surface effects*, J. Phys. D-Appl. Phys. **42**, 5 (2009).
- [12] V. B. Shenoy, *Atomistic calculations of elastic properties of metallic fcc crystal surfaces*, Phys. Rev. B **71**, 094104 (2005).
- [13] C.-L. Hsin, W. Mai, Y. Gu, Y. Gao, C.-T. Huang, Y. Liu, L.-J. Chen and Z.-L. Wang, *Elastic Properties and Buckling of Silicon Nanowires*, Adv. Mater. **20**, 3919 (2008).
- [14] J. W. Gibbs, *Scientific Papers of J. Willard Gibbs: Vol.1 Thermodynamics* (Longmans, Green and Company, 1906).
- [15] R. C. Cammarata, T. M. Trimble and D. J. Srolovitz, *Surface stress model for intrinsic stresses in thin films*, J. Mater. Res. **15**, 2468 (2000).
- [16] G. Y. Jing, H. L. Duan, X. M. Sun, Z. S. Zhang, J. Xu, Y. D. Li, J. X. Wang and D. P. Yu, Surface effects on elastic properties of silver nanowires: Contact atomic-force microscopy, Phys. Rev. B 73, 6 (2006).
- [17] R. E. Miller and V. B. Shenoy, *Size-dependent elastic properties of nanosized structural elements*, Nanotechnology **11**, 139 (2000).
- [18] G. F. Wang and X. Q. Feng, Surface effects on buckling of nanowires under uniaxial compression, Applied physics letters **94**, 3 (2009).
- [19] G. F. Wang and X. Q. Feng, *Effects of surface elasticity and residual surface tension on the natural frequency of microbeams*, Applied physics letters **90**, 3 (2007).
- [20] J. He and C. M. Lilley, Surface stress effect on bending resonance of nanowires with different boundary conditions, Applied physics letters **93**, 3 (2008).
- [21] S. P. Timoshenko and J. M. Gere, *Theory of Elastic Stability*, 2nd ed., ISBN-10: 0486472078 (McGraw-Hill, New York, 1961).

- [22] G. F. Wang and F. Yang, *Postbuckling analysis of nanowires with surface effects*, J. Appl. Phys. **109**, 4 (2011).
- [23] P. F. Byrd and M. D. Friedman, *Handbook of elliptic integrals for engineers and physicists*, 2nd ed., ISBN-10: 0387053182 (Springer, Berlin, 1954).
- [24] T. F. Lemczyk and M. M. Yovanovich, *Efficient evaluation of incomplete elliptic integrals and functions*, Comput. Math. Appl. **16**, 747 (1988).
- [25] A. Schett, *Properties of the Taylor series expansion coefficients of the Jacobian elliptic functions*, Mathematics of Computation **30**, 143 (1976).
- [26] M. Luisier and G. Klimeck, Simulation of nanowire tunneling transistors: From the Wentzel-Kramers-Brillouin approximation to full-band phonon-assisted tunneling, J. Appl. Phys. 107, 6 (2010).
- [27] T. Taketsugu and K. Hirao, *A least-action variational method for determining tunneling paths in multidimensional system*, J. Chem. Phys. **107**, 10506 (1997).
- [28] R. Nandkishore and L. Levitov, *Common-path interference and oscillatory Zener tunneling in bilayer graphene p-n junctions*, Proc. Natl. Acad. Sci. U. S. A. **108**, 14021 (2011).
- [29] M. Razavy, *Quantum theory of tunneling*, ISBN-10: 9812380813 (World Scientific, Singapore, 2003).
- [30] J. G. Simmons, Generalized formula for the electric tunnel effect between similar electrodes separated by a thin insulating film, J. Appl. Phys. **34**, 1793 (1963).
- [31] D. B. Williams and C. B. Carter, *Transmission Electron Microscopy: A Textbook for Materials Science*, ISBN-10: 030645324X (Plenum, New York, 1996).
- [32] R. F. Egerton, *Electron Energy-Loss Spectroscopy in the Electron Microscope*, 2nd ed., ISBN-10: 0306452235 (Plenum, New York, 1996).
- [33] M. M. Balakrishnarajan, P. D. Pancharatna and R. Hoffmann, *Structure and bonding in boron carbide: The invincibility of imperfections*, New J. Chem. **31**, 473 (2007).

- [34] V. Domnich, S. Reynaud, R. A. Haber and M. Chhowalla, *Boron Carbide: Structure, Properties, and Stability under Stress*, J. Am. Ceram. Soc. **94**, 3605 (2011).
- [35] L. X. Dong, X. Y. Tao, L. Zhang, X. B. Zhang and B. J. Nelson, *Nanorobotic spot welding: Controlled metal deposition with attogram precision from copper-filled carbon nanotubes*, Nano Lett. **7**, 58 (2007).
- [36] C. Kittel, *Introduction to solid state physics*, 7th ed., ISBN-10: 0471111813 (Wiley, New York, 1996).
- [37] N. Hong, M. A. Langell, J. Liu, O. Kizilkaya and S. Adenwalla, *Ni doping of semiconducting boron carbide*, J. Appl. Phys. **107**, 7.
- [38] X. Tao, L. Dong, X. Wang, W. Zhang, B. J. Nelson and X. Li, *B4C Nanowires/Carbon-Microfiber Hybrid Structures and Composites from Cotton T-shirts*, Adv. Mater. **22**, 2055 (2010).
- [39] V. V. Sokolov and V. G. Zelevinsky, *Collective Dynamics of Unstable Quantum States*, Annals of Physics **216**, 323 (1992).
- [40] A. Volya and V. Zelevinsky, *Superradiance and open quantum systems*, paper presented at the AIP Conference Proceedings (2005).
- [41] S. Sorathia, F. M. Izrailev, V. G. Zelevinsky and G. L. Celardo, From closed to open one-dimensional Anderson model: Transport versus spectral statistics, Physical Review E 86, 011142 (2012).
- [42] G. Shchedrin and V. Zelevinsky, *Resonance width distribution for open quantum systems*, Physical Review C **86**, 044602 (2012).